Planar Wire Array Performance Scaling at Multi-MA Levels on the Saturn Generator

Brent Jones, Michael E. Cuneo, David J. Ampleford, Christine A. Coverdale, Eduardo M. Waisman, Roger A. Vesey, Michael Jones, Andrey A. Esaulov, Victor L. Kantsyrev, Alla S. Safronova, Alexandre S. Chuvatin, Leonid I. Rudakov

Sandia National Laboratories

Planar Wire Array Performance Scaling at Multi-MA Levels on the Saturn Generator

B. Jones
Z Experiments

M.E. Cuneo
Z Experiments

D.J. Ampleford
Z Experiments

C.A. Coverdale
Radiation Effects Research

E.M. Waisman
Z Experiments

R.A. Vesey
ICF Target Design

M. Jones
Z Diagnostics

Sandia National Laboratories
P.O. Box 5800
Albuquerque, NM 87185

A.A. Esaulov
Department of Physics

V.L. Kantsyrev
Department of Physics

A.S. Safronova
Department of Physics

University of Nevada, Reno
Reno, NV 89557

A.S. Chuvatin
Laboratoire de Physique et Technologie des Plasmas

Laboratoire du Centre National
de la Recherche Scientifique
Ecole Polytechnique
91128 Palaiseau, France

L.I. Rudakov

Icarus Research
P.O. Box 30780
Bethesda, MD 20824-0780

Abstract

A series of twelve shots were performed on the Saturn generator in order to conduct an initial evaluation of the planar wire array z-pinch concept at multi-MA current levels. Planar wire arrays, in which all wires lie in a single plane, could offer advantages over standard cylindrical wire arrays for driving hohlraums for inertial confinement fusion studies as the surface area of the electrodes in the load region (which serve as hohlraum walls) may be substantially reduced. In these experiments, mass and array width scans were performed using tungsten wires. A maximum total radiated x-ray power of 10±2 TW was observed with 20 mm wide arrays imploding in ∼100 ns at a load current of ∼3 MA, limited by the high inductance. Decreased power in the 4-6 TW range was observed at the smallest width studied (8 mm). 10 kJ of Al K-shell x-rays were obtained in one Al planar array fielded. This report will discuss the zero-dimensional calculations used to design the loads, the results of the experiments, and potential future research to determine if planar wire arrays will continue to scale favorably at current levels typical of the Z machine. Implosion dynamics will be discussed, including x-ray self-emission imaging used to infer the velocity of the implosion front and the potential role of trailing mass. Resistive heating has been previously cited as the cause for enhanced yields observed in excess of **j**x**B**-coupled energy. The analysis presented in this report suggests that **j**x**B**-coupled energy may explain as much as the energy in the first x-ray pulse but not the total yield, which is similar to our present understanding of cylindrical wire array behavior.

Acknowledgment

Contents

List of Figures

List of Tables

Chapter 1

Introduction

Wire array z pinches are bright, efficient soft x-ray sources, producing up to 250 TW and 1.8 MJ of radiation [1] in experiments on Sandia's Z machine [2]. Z-pinch loads are used for a variety of high energy density physics applications, including inertial confinement fusion (ICF) studies, K-shell x-ray generation for radiation effects research, and radiation and atomic physics [3]. These loads are typically high wire number ($N{\sim}300$) annular arrays with initial diameters in the 20-60 mm range. A high level of azimuthal symmetry (i.e. high wire number in a cylindrically symmetric configuration) is believed to be important in producing high x-ray powers as a symmetrical implosion produces a more uniform shell with smaller radial width, better convergence of the mass and current, and a higher level of mass participation in x-ray production [4, 5].

Recently, planar wire array configurations, in which the wires are arranged as a linear array confining the mass within a plane, have attracted attention in the z-pinch community. Experiments on the 1 MA Zebra generator at the University of Nevada, Reno, produced implosions with < 10 ns x-ray rise times and powers as high as 0.34 TW/cm, comparable to the most powerful cylindrical wire array implosions studied at that facility [6]. This behavior is surprising, as the standard intuition regarding cylindrical arrays is that high implosion velocity and a radially narrow plasma shell are required to achieve a fast rising and high power x-ray pulse. The planar array distributes the initial mass profile radially, which is not intuitively optimal for providing high implosion velocity. Laser shadowgraphy indicates, however, that the wires implode in a cascade, with magnetic Rayleigh-Taylor implosion instabilities being stabilized to some extent as the implosion front impacts each adjacent wire on its way toward the axis [7]. This may suggest that a linear array mitigates instabilities as a multiply nested wire array; nested cylindrical wire arrays have been previously demonstrated to enhance the radiated x-ray power and shorten the pulse due to mitigation of the magnetic Rayleigh-Taylor implosion instability [1] as the current is switched from the outer to the inner array during the implosion [8].

Previous publications have also discussed the possibility of enhanced Ohmic heating due to Hall resistivity effects in wire array z pinches, suggesting that the effect might be exaggerated and thus more clearly observable in planar arrays versus cylindrical arrays due to a smaller amount of coupled kinetic energy in the planar array case [9, 6].

Numerical modeling of wire arrays with a three-dimensional (3D) magnetohydrodynamic (MHD) code has indicated that resistive heating can play a role in cylindrical wire array energy deposition, but this contribution is strongest and dominant only after the main x-ray peak [10]. These simulations assumed Spitzer resistivity, however, and would not have reflected the effects of enhanced resistivity due to Hall physics if in fact this phenomenon occurs and is significant in modifying the pinch energetics. If planar arrays offer an opportunity to assess the role of Ohmic heating in wire array plasmas, this insight would be generally beneficial to our understanding of z-pinch physics.

A linear array of wires has also been used to study wire ablation physics, with an asymmetric single return current post providing a global magnetic field [11]. Plasma was ablated perpendicular to the plane of the array in a manner consistent with inductive current division between the wires in this work.

Planar arrays are thus interesting objects from a z-pinch physics perspective, and their study may shed light on instability mitigation and plasma heating mechanisms. Beyond basic physics issues, these arrays may be particularly attractive for ICF research due to the reduced volume occupied by the initial load configuration. The double-ended vacuum hohlraum z-pinch-driven ICF concept [12] which has been extensively studied on the Z machine [13] relies on a cylindrical primary hohlraum which also serves as the return current canister for the z-pinch radiation source on axis. The surface area of the hohlraum is thus constrained by the initial geometry of the cylindrical wire array. For a fixed x-ray pulse shape, the peak radiated power required to produce a given peak hohlraum temperature is given by the relation [14]

$$P \propto \left(R^2 + RL \right)^{1.1} \tag{1.1}$$

which depends strongly on the hohlraum surface area (R is its radius and L is the length). The hohlraum temperature requirement is typically fixed by the design of the fuel capsule which resides in a secondary hohlraum driven from either end by two z-pinch-driven primary hohlraums. Thus, reducing the hohlraum area (radius in particular) is attractive for reducing the power requirement placed on the z-pinch radiation source. The reduction of the wire array area from a cylindrical to a planar geometry may allow for a significant reduction in primary hohlraum area (the area of a rectangular current return electrode), as one dimension can be as thin as twice the anode-cathode feed gap width and no longer has to be wider than the array diameter. This advantage assumes that planar wire arrays retain their relatively fast rise times and high powers as they are scaled up to higher drive currents, which is a prime motivation for the experiments on Saturn discussed in this report. We note that planar arrays are not required to outperform cylindrical wire arrays–if there is in fact a reduction in x-ray power, this might be offset by the potential reduction in primary hohlraum area. Ultimately, x-ray power scaling experiments must be complemented by integrated hohlraum and capsule modeling in order to determine whether planar-

array-driven hohlraum energetics competes with the use of compact cylindrical wire array sources.

Due to the relatively short path lengths through the plasma in the direction normal to the plane, planar wire arrays may also offer an advantage in mitigating opacity effects which could limit peak radiated power in high mass, high current, cylindrical implosions [15].

A final motivating factor is the report from the GIT-12 generator (4.7 MA, 1.7 μs implosion time) of an increase in Al K-shell yield by a factor of $\sim$2 compared to previous cylindrical arrays studied [16]. Wire arrays for producing K-shell x-rays are typically larger diameter than the compact ICF loads, placing the mass at large initial diameter so that high implosion velocities and thus plasma temperatures can be achieved for ionizing to the K shell [17]. It is arguably even less intuitive that planar wire arrays would benefit K-shell x-ray production, as the mass is radially distributed rather than initiated at large diameter, but this is another topic that can be addressed on Saturn.

The following section describes the shot plan and experimental goals for the May-June 2007 Saturn planar wire array series, including the zero-dimensional (0D)-type code used to aid in pre-shot load design and post-shot analysis. The x-ray diagnostics used for these shots are also described. The third chapter presents the experimental results, including tungsten power scaling experiments for ICF applications, planar array dynamics and energetics analysis, and Al K-shell x-ray production from a planar wire array. A concluding chapter summarizes the results and discusses possible future experiments to assess more fully the power scaling prospects of planar wire arrays. Primary goals in this report are to provide fairly complete documentation of the experiments in order to facilitate ongoing collaborations, to outline near-term analysis goals, and to discuss future directions for study of planar wire arrays.

Chapter 2

Planar Wire Array Experiment Design

A primary design goal in fielding these experiments at Saturn was to match the implosion time to that expected on the Z machine (100-120 ns) in order to most reliably consider x-ray power scaling with load current for planar arrays. In addition, an implosion time near 100 ns would be well matched to prior [6] and future experiments at 1 MA on the Zebra generator, and so these data points could be considered in a power scaling study. As such, we chose to run Saturn in long-pulse mode, which has previously been used to study cylindrical arrays with 130-250 ns implosion times [18, 19]. The Saturn short-pulse mode [5] typically exhibits a peak in the load current waveform at < 60 ns, which is too short for the desired planar array regime. A new, larger 12 inch diameter convolute design for Saturn long-pulse mode was fielded as there is evidence that this convolute has superior powerflow properties and handles high inductance loads better than the traditional 6 inch convolute [20].

In the early stages of load hardware design, it was decided to be very conservative with the anode-cathode gap spacing both in the inner MITL feed and in the return current cage surrounding the wire array load (see Figs. 2.1, 2.2) to reduce risk of load current arcing. 6-7 mm feed gaps were chosen as the Saturn MITL alignment accuracy is presently limited. The circuit-coupled 0D-type calculations described below were performed later in shot planning process (too late to make significant changes to the load hardware design and still complete the experiments during the FY07 LDRD cycle). These calculations indicated high load inductances that, when coupled with the fairly high inner MITL inductances and the 100-120 ns desired implosion time in the Saturn circuit, led to a roll-over of the load current at levels of ~ 3 MA. Only by taking the implosion time out to 200 ns could this load hardware design approach the 6 MA current level that was desired in these studies. Thus, the conservative gap spacing forced an undesirable but unavoidable trade-off between load current and implosion time. The compromise chosen was to select the wire size and thus load mass with predicted implosion times near nominally 135 ns, giving load currents of ~ 3 MA. This still puts the experiments in the multi-MA range significantly above 1 MA and allows us to start to consider power scaling, but does not achieve the ~ 6 MA levels desirable of more direct relevance to ICF concepts using planar wire arrays on Z. This planned implosion time is somewhat longer than Zebra at 100 ns, and slightly
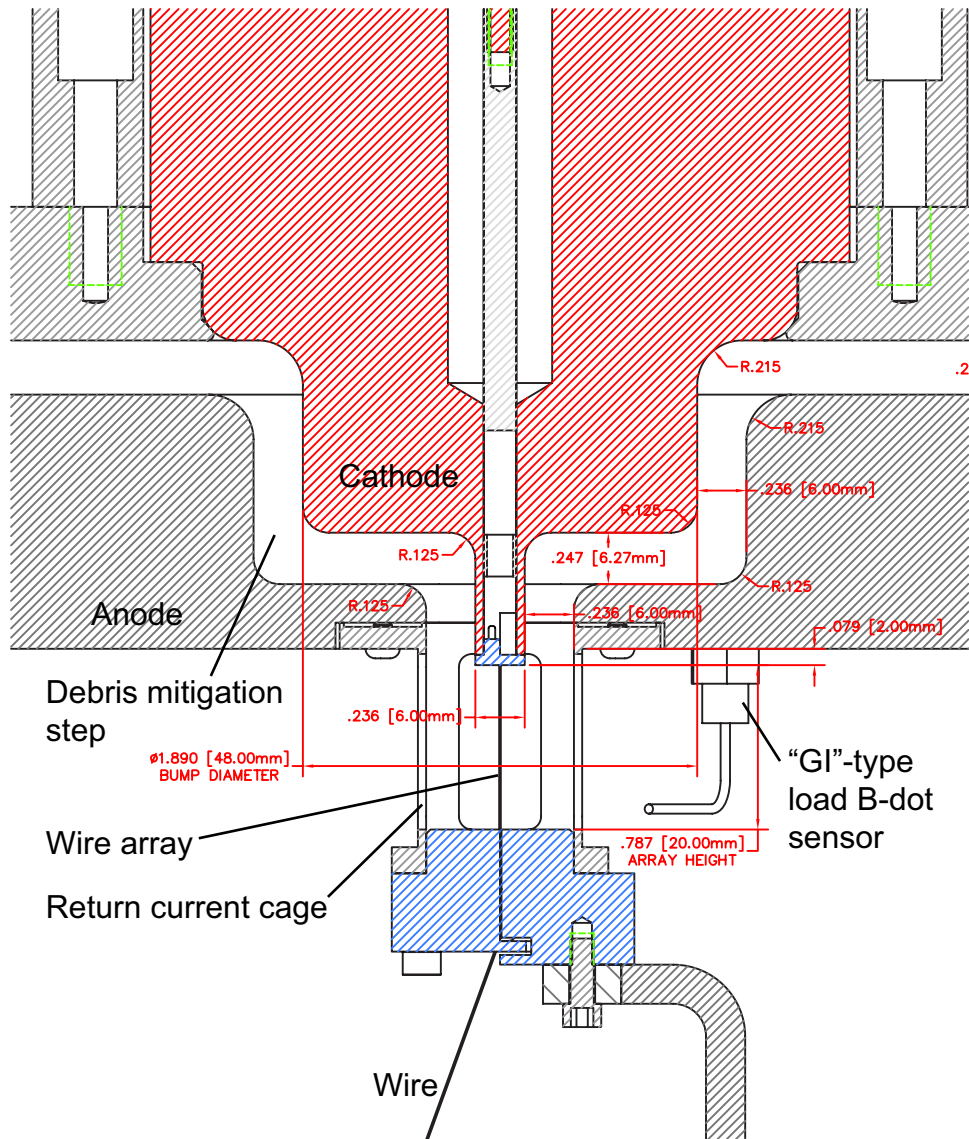
Figure 2.1. Drawing of the load region for the hardware design used in the May-June 2007 planar array Saturn shot series, courtesy of M.D. Kernaghan (1672) and M. Vigil (1675). The view here is parallel to the array of wires. Design requirements included a debris mitigation step feature in order to evaluate an option for multiple shots per day without MITL cleaning, as well as another debris mitigation bump (not shown). These features increased the load inductance, may not actually permit a higher shot rate (see the text for discussion), and can be eliminated to decrease load inductance.

Cathode

ø1.890 [48.00mm]

.236 [6.00mm]

Anode

.260 [6.60mm]

R.215

R.215

R.125

R.125

R.125

R.125

Return current cage

Wire array

.787 [20.00mm]
ARRAY HEIGHT

.247 [6.27mm]

.079 [2.00mm]

Debris mitigation step

1.102 [28.00mm]
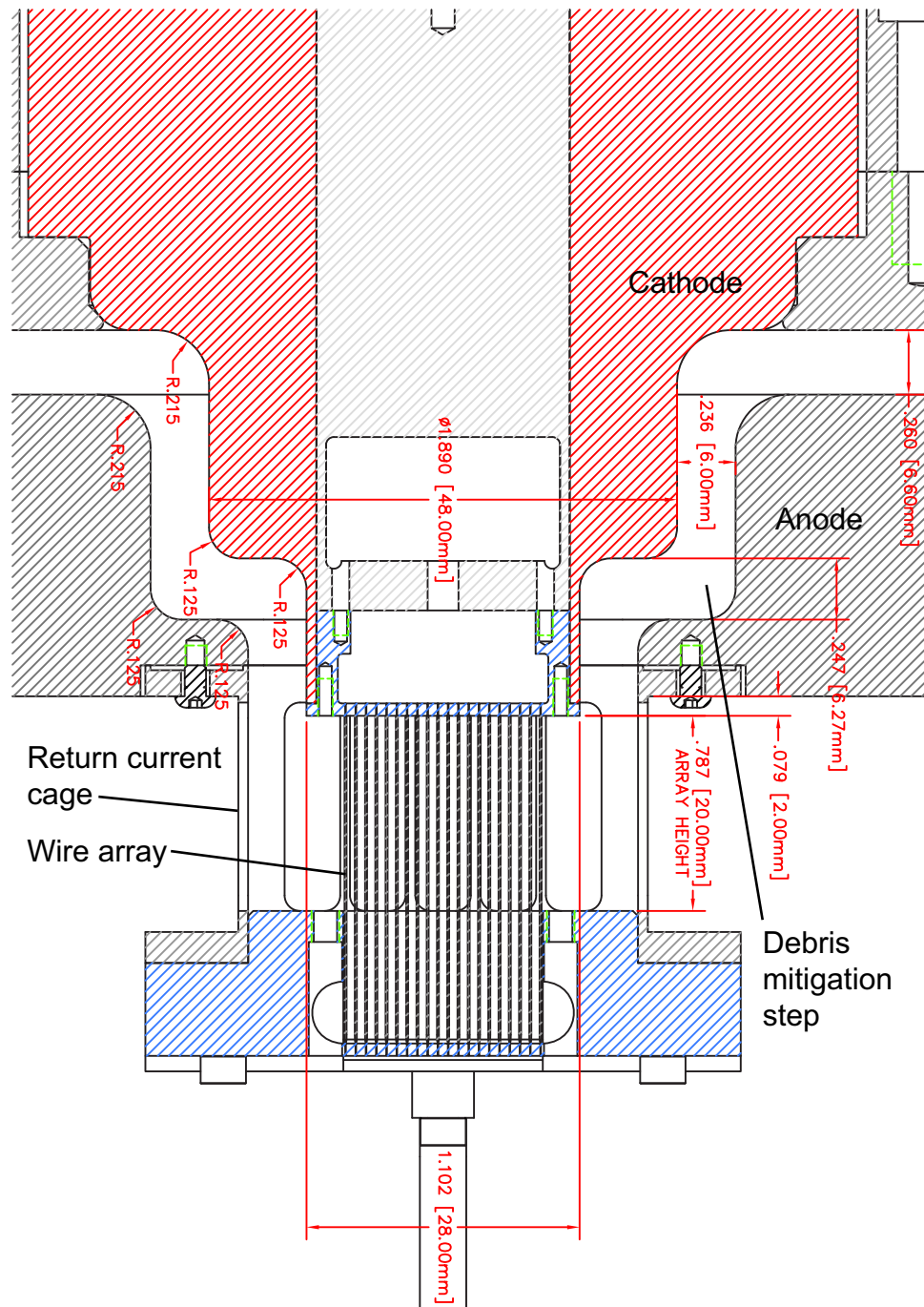
Figure 2.2. Drawing of the load region for the hardware design used in the May-June 2007 planar array Saturn shot series, courtesy of M.D. Kernaghan (1672) and M. Vigil (1675). The view here is perpendicular to the array of wires. A 20 mm wide wire array is shown, but the same load hardware was used for all wire array initial widths studied. The gaps in the load region are very conservative and may possibly be reduced to 2-4 mm based on other work [21] to decrease the load inductance.

Table 2.1. Planar wire array design parameters from the May-June 2007 Saturn shot series. Table 2.2 lists calculated implosion times, load currents, and coupled energies, while Table 3.1 lists experimental results.

Shot number	Wire material	Array height, h (mm)	Array width, W (mm)	Wire number	Wire diameter (μm)	Array mass (mg/cm)	Design implosion time
3670	W	20	20	40	9.09	0.500	Nominal
3671	W	20	20	40	6.41	0.248	Early
3672	W	20	20	40	12.86	1.000	Late
3673	W	20	20	40	12.86	1.000	Late
3674	W	20	20	40	9.09	0.500	Nominal
3675	W	20	20	40	25.58	3.957	Very late
3682	W	20	20	40	9.09	0.500	Nominal
3683	W	20	8	16	28.21	1.925	Nominal
3684	W	20	12	24	19.25	1.345	Nominal
3685	W	20	12	24	19.25	1.345	Nominal
3686	W	20	8	16	28.21	1.925	Nominal
3688	Al 5056	20	20	40	23.60	0.472	Nominal

longer than the expected nominal short-pulse operating point of the refurbished Z machine at 120 ns. However, as will be presented below, the implosion times that were measured experimentally turned out to be closer to 100 ns.

These experiments were designed to determine the scaling of peak x-ray power and x-ray energy in the main pulse of planar arrays for application to ICF research. The critical scalings are (1) with implosion time at constant array width (this is a mass scan), (2) with array width at fixed implosion time, and (3) with peak drive current at constant implosion time and width. Saturn data are used to evaluate (1) and (2). Issue (3) is evaluated using data both from Saturn and from the University of Nevada, Reno, Zebra generator at 1 MA.

Twelve shots were planned and executed on Saturn during May-June 2007. The load parameters for this series are specified in Table 2.1. As will be discussed in the experimental results section, shots 3673, 3674, and 3685 were compromised and will not be used in the scaling studies. The series was designed to accomplish three basic experiments. First, shots 3670, 3682, 3683, and 3686 comprise a mass (and implosion time) scan at fixed planar array width. The goal here is to determine empirically the optimum implosion time for maximizing peak x-ray power with the chosen load hardware geometry. We also wish to study how the load behaves with longer implosion times but greater coupled energy (one shot, 3675, was planned with implosion time near 200 ns and load current in the 5 MA range). Second, shots

3670, 3682, 3683, 3684, and 3686 comprise a width scan where the implosion time was kept near the nominal 135 ns value but the array size was reduced. The goal with this set is to determine how compact the array can be made before the x-ray power drops significantly. In addition, the **jxB**-coupled energy was expected to vary over these shots, and we hoped to address the question of whether this can explain the measured yields, or whether it is necessary to invoke resistive heating. Finally, one shot, 3688, will provide preliminary information on how effective planar wire arrays are at producing K-shell x-rays at multi-MA current. For all of these shots, a series of electrical and x-ray power, yield and imaging diagnostics were fielded as described below to study the planar array implosion dynamics and attempt to make some statement about energy coupling.
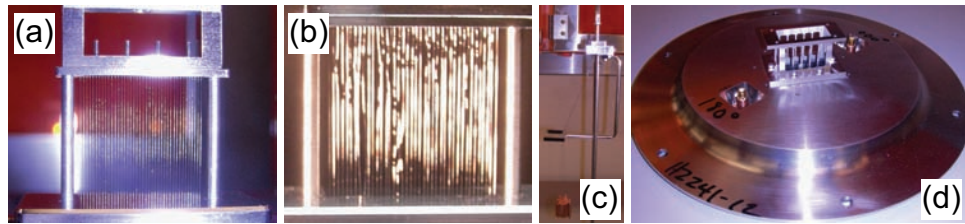
Figure 2.3. Photographs of load hardware from the May-June 2007 Saturn planar array shots. (a) A 20 mm wide, 20 mm tall, 40-wire W array. (b) A 20 mm wide, 20 mm tall, 40-wire Al 5056 array; the Al 5056 wires hung noticeably less straight than the W wires. (c) Lower halo assembly and hanging weights keep the wires under tension. (d) Anode insert showing the B-dot sensors at 0° and 180°, and the return current cage. Courtesy of S.P. Toledo (1676).

Figure 2.3 includes photographs of load hardware for the reader's reference. The tungsten wires generally hung quite straight, but the Al 5056 wires in shot 3688 were somewhat crooked due to the thickness of the wire used. The aluminum wire is more fragile than the tungsten, and thus it could not be put under greater tension without an unacceptable amount of wire breakage during assembly. Figure 2.3(c) shows the weighted wires hanging over a lower halo-type assembly which served to keep the wires under tension, reduce swinging of weights during transport, and pull the wires into current contact with the anode. The halo design and wire hanging features are similar to those used with a single-feed double z-pinch array on Z. During assembly, each wire was wrapped around one of the four vertical posts shown at the top of Fig. 2.3(a) with both weighted ends hanging down to become two wires in the planar array. The small radius of these posts posed problems with wire handling and breakage. It was also difficult to position the wires in the EDM-cut slots on the cathode when working near the edges of the wire array due to the proximity of the vertical bars shown at the top of Fig. 2.3(a). The assembly of these loads was somewhat more difficult than typical cylindrical wire arrays, and indeed a number of issues were identified that

should be considered in designing any future planar array load hardware [courtesy of D. A. Graham (1676)].

The return current canister, important in determining the load inductance, was a rectangular cage as shown in Fig. 2.3(d). In order to minimize hardware costs for these shots, the same load hardware was used for all shots with the only difference being the pattern of EDM-cut wire slots in the anode and cathode. As such, the return current cage was much larger than necessary for the 12- and 8-mm-width arrays. Inductance could be reduced in future shots by reducing anode-cathode gaps in the inner MITL and in the cage, which might serve to increase load current.

For all shots, an inter-wire gap near 0.5 mm was chosen. This decision was made in order to facilitate assembly of the loads, but also because prior work with cylindrical wire arrays has indicated that too small an inter-wire gap can be detrimental to x-ray power performance [19, 22]. The mechanism for degradation has been speculated to be due to an unfavorable modification of the ablated plasma pre-fill profile as wire number is changed [23] or a merging of the current-carrying coronal plasma surrounding the wires early in time, allowing current to jump between adjacent wires and compromising the uniformity of the current path [24]. It is not clear that either of these mechanisms would be relevant to planar wire arrays, which already have a significant initial mass distribution interior to the load, and in which the current distribution between the wires is likely inductive with stronger current density on the outer edges of the array. Also, unpublished experiments with planar arrays at 1 MA at the University of Nevada, Reno, showed that power decreased for inter-wire gaps of both 0.2 mm and 1 mm compared to 0.5 mm [25].

Given these physics concerns and the practical concerns associated with building the loads, we fixed the inter-wire gap near 0.5 mm which placed a constraint on the parameter space of the load design. This choice, coupled with the choice of array widths and implosion times in Table 2.1, resulted in some loads having relatively large wire sizes approaching 30 μm diameter. This in itself poses a concern regarding wire initiation and ablation behavior, and clearly future experiments with higher wire number and smaller inter-wire gaps could be interesting. Planar arrays tend to have large mass relative to cylindrical arrays of the same spatial scale and implosion time due to the initial distribution of this mass near the array axis, which is what leads to the increased wire size requirement. We note also that for high-current planar array experiments it might be possible to consider using a foil ribbon in place of a planar wire array, which would certainly change the ablation and perhaps implosion dynamics.

Pre-shot 0D-type modeling for load design

The load widths and implosion times were chosen to meet experimental goals as discussed above. With the inter-wire gap also fixed, the remaining as-yet-unspecified design parameter is the wire size. This must be chosen to give the array the appropriate mass so that the appropriate implosion time will be achieved when coupled to the generator. In the case of cylindrical wire arrays, 0D thin-shell calculations are typically employed in load design calculations to choose the load mass [26]. Here, the wire array is approximated as a zero-thickness shell of mass, and the radial equation of motion is solved numerically in the azimuthally symmetric case while also coupling the evolution of the load inductance to the generator circuit. This calculation is less straightforward for a planar array, which lacks cylindrical symmetry and for which load inductance is a more complicated function of geometry than the cylindrical case, where $L \sim 2h \; log(R/r)$ for a wire array of height h, radius r and return current canister radius R. A technique for performing a 0D-type simulation for an arbitrary arrangement of wires and return current structures has been developed, however, and was employed in collaboration with A. A. Esaulov (University of Nevada, Reno) in designing the planar array loads for the May-June 2007 Saturn shots. Termed the "wire dynamics model" [27], the technique can be applied to single or multiply nested cylindrical arrays, or planar wire arrays. The model implicitly includes inductive division of current between the wires at each time step, and essentially applies F=ma to each wire in order to track its trajectory. Inductive current division still allows current to be distributed throughout the wires in a planar array, but causes current to peak in the few wires near the edge of the array with the outermost wires carrying a factor of 2-3 times more current than the innermost wires [27]. We expect this to be the most reasonable assumption for planar arrays, given the observations that the inner wires ablate and so must carry some current [6], but also that the inner wires experience little acceleration while the implosion commences at the outer wires and cascades inward [7] implying that somewhat less current flows in the inner wires. Modeling with inductive division best reproduces the latter observation. We note, however, that modeling of the planned Saturn planar loads was also carried out by A. S. Chuvatin (Ecole Polytechnique) with the assumption of uniform (i.e. resistive) current division between the wires, and similar implosion times, peak currents, and coupled energies were obtained.

The 0D planar array simulations included coupling to the Saturn circuit model shown in Fig. 2.4. The voltage at the post-hole convolute was estimated using the expression

$$V_{PH} = \begin{cases} +Z_f \sqrt{I_u^2 - I_d^2}, \text{ Rising current: } I_d < I_u \\ -Z_f \sqrt{I_d^2 - I_u^2}, \text{ After peak: } I_d > I_u \end{cases} \qquad (2.1)$$

The inner MITL inductance was calculated as described in Fig. 2.5. The load inductance was calculated internally in the 0D code, including inductive division between
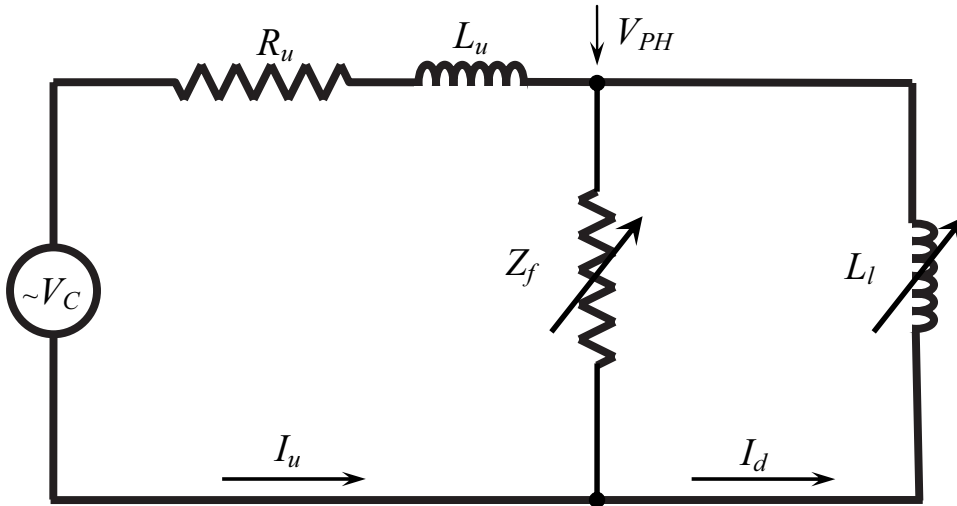
Figure 2.4. The Saturn generator was modeled with the equivalent circuit shown in performing 0D-type implosion calculations. R_u=0.15 Ω is expected for Saturn with 36 modules, but R_u=0.2 Ω was used here as the May-June 2007 shots were conducted with only 30 modules. Z_f=0.25 Ω was assumed, Eq. 2.1 was used for V_{PH}, and L_u=5 nH. Courtesy of A. A. Esaulov (University of Nevada, Reno).

wires and appropriate boundary conditions on the return current cage to determine its current distribution. The return current cage was modeled as a series of stationary filaments, as shown in Fig. 2.6(a). Figure 2.6(c-e) shows magnetic field lines within the load region for the initial configurations of planar arrays of 8, 12, and 20 mm width as calculated by the code. The initial calculated load inductances are indicated, and are seen to be quite high due to the geometry of the magnetic field and the size of the return current structure. These initial load inductances were also verified by electromagnetic calculations with a more accurate return current cage geometry (Fig. 2.7). In the case of the smaller width loads in Fig. 2.6, it is clear that the return current cage is excessively large, leading to a large volume filled with magnetic energy and correspondingly a large inductance. Again, this was because the same load hardware was used for all shots in order to reduce costs. Future experiments with a more closely coupled return current can could be designed in order to reduce the inductance and increase the load current. Figures 2.6(c-e) also give some intuition as to why the implosion starts in the outer wires and cascades through the stationary inner wires–tension in the magnetic field lines is greatest at the edges of the array where curl of **B** (and hence **j** and then also **j**x**B**) is large. Figure 2.7(a) indicates that the magnetic pressure is greatest at the edges of the array as well.

Figure 2.6(b) shows an example of implosion calculations for wire arrays of various widths, designed so that they have the same implosion time. Here x indicates the

h=0.627cm, R=15.2cm, r=2.4cm
L~2h ln(R/r)~2.32 nH

h=1.7cm, R=3cm, r=2.4cm
L~2h ln(R/r)~0.76 nH

h=0.627cm, w=2.8cm, R=3cm
L~2h ln(4R/w)~1.83 nH

h=1cm, w=2.8cm, d=0.6cm
L~4πhd/(2w)~1.35 nH
More exact L~0.91 nH

Load inductance calculated
in 0D implosion code
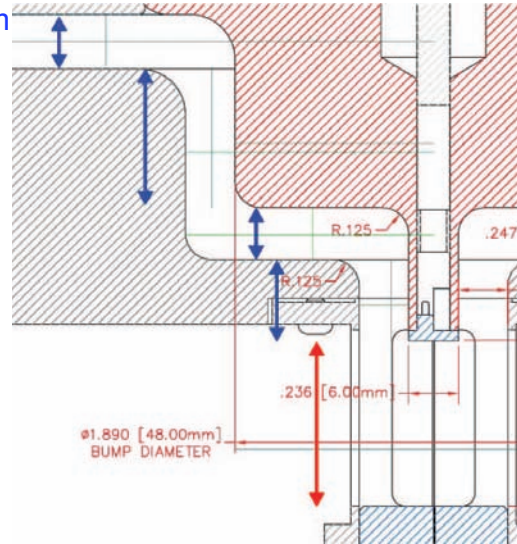
Figure 2.5. The inner MITL inductance for the load hardware used in May-June 2007 Saturn planar array shots was calculated as shown. The inductance of a cylindrically symmetric MITL section is estimated with the standard formula $L \sim 2h \, log \, (R/r)$, where h is the height, R is the outer radius, and r is the inner radius. The inductance of each strip line section is estimated as $L \sim 4\pi hd/(2w)$, where h is the height, w the width, and d is the anode-cathode gap spacing, and the expression is valid for d≪w; the factor of 2 accounts for the two current returns. A more exact analytic treatment was also applied to the strip line sections [28]. A net inner MITL inductance of 5 nH was then used for all of these shots in 0D-type implosion calculations. Courtesy of A. S. Chuvatin (Ecole Polytechnique).
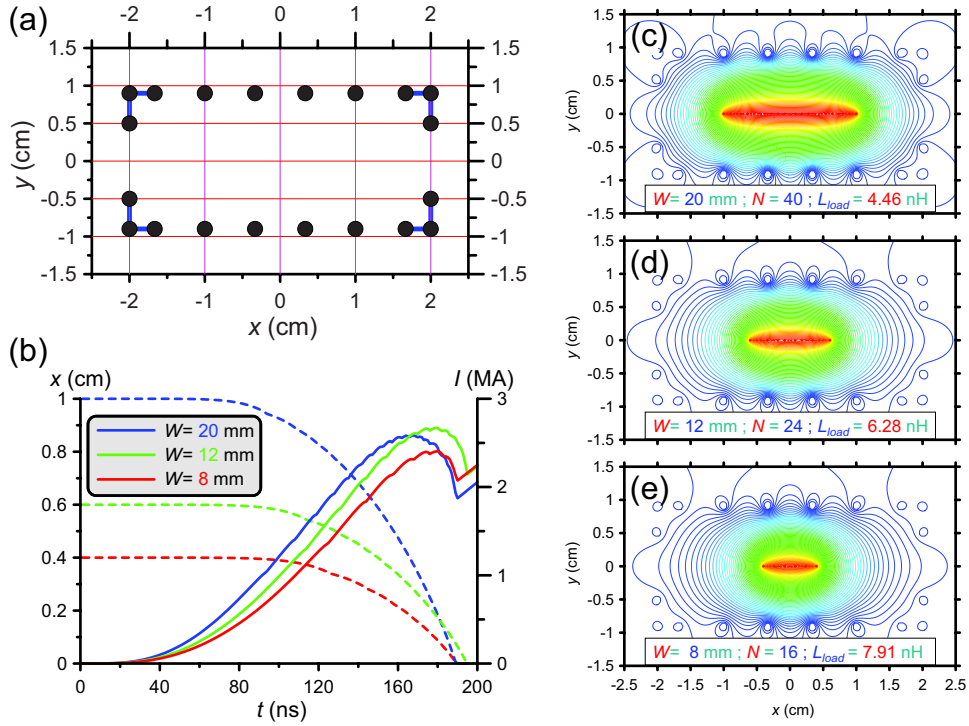
Figure 2.6. Planar array load design was aided by 0D-type calculations of trajectory and current. (a) The return current cage was modeled as a set of current filaments (black circles). (b) Load mass was chosen here for constant implosion time at several array widths W and wire numbers N. (c-d) Magnetic field lines for initial load configurations at various W, N; initial inductance L_{load} is calculated assuming inductive current division between the wires. Courtesy of A. A. Esaulov (University of Nevada, Reno).
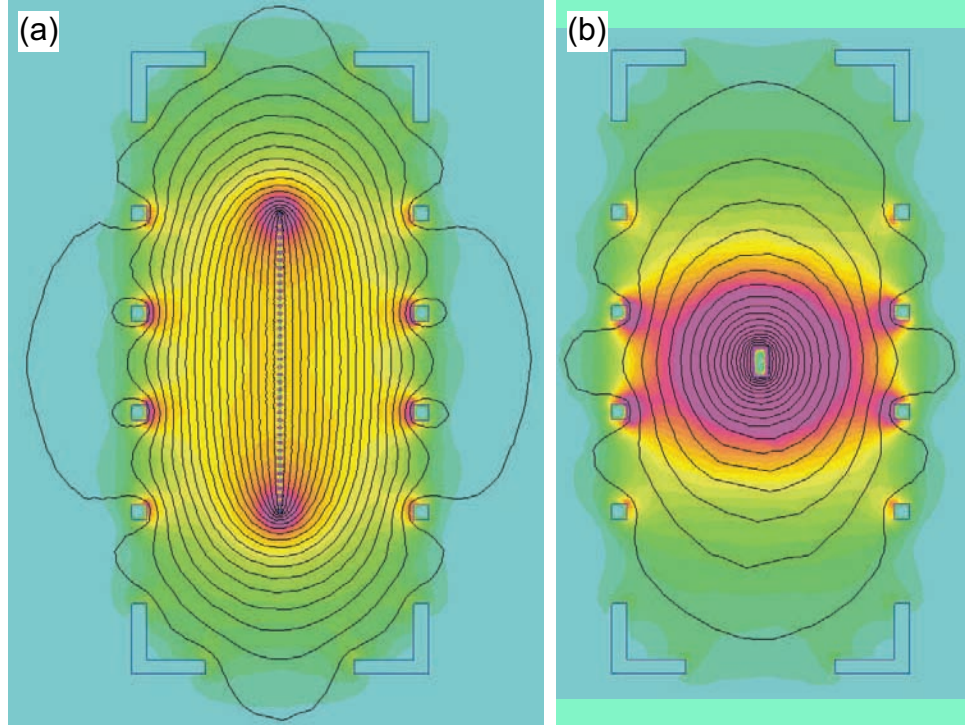
Figure 2.7. (a) An electromagnetic code calculation of initial load inductance with accurate return current cage geometry gives 4.26 nH for an array of 20 mm width, in close agreement with the simplified cage model of Fig. 2.6(c). (b) The inductance rises to 10.63 nH for a z-pinch current channel compressed to 2 mm × 1 mm, a convergence ratio of 10. The magnetic field lines are shown along with color contours indicating field strength. This figure also indicates that the load inductance will be most sensitive to the feed gap spacing in the direction perpendicular to the wire array; the configuration of the cage bars may also be important. Courtesy of A. S. Chuvatin (Ecole Polytechnique).

Table 2.2. Predicted planar wire array load behavior, calculated with a 0D-type code including a Saturn circuit model in advance of the experiments and used to guide the choice of load parameters in Table 2.1. Table 3.1 lists experimental results for comparison. Courtesy of A. A. Esaulov (University of Nevada, Reno).

Shot number	Design implosion time	Implosion time (ns)	Peak load current (MA)	Coupled energy (kJ) $(x_f = 100\mu m)$
3670	Nominal	138	2.5	41
3671	Early	124	2.0	25
3672	Late	152	3.0	64
3673	Late	152	3.0	64
3674	Nominal	138	2.5	41
3675	Very late	200	4.7	140
3682	Nominal	138	2.5	41
3683	Nominal	125	2.3	34
3684	Nominal	135	2.5	44
3685	Nominal	135	2.5	44
3686	Nominal	125	2.3	34
3688	Nominal	137	2.5	39

position of the outermost wire which becomes the implosion front as it sweeps up the mass held in the interior wires. This code does not include wire ablation, which could impact the implosion trajectory by influencing when the outer wire begins to move. Given the large amount of mass already interior to the implosion front in a planar array, we might expect ablation to play less of a role in the dynamics and energy coupling than in a compact cylindrical wire array; this is a topic of continuing research, however. Figure 2.6(b) also shows the calculated load current resulting from coupling the wire array trajectory calculations with the Saturn circuit model in Fig. 2.4. It is seen that the large load inductance and short implosion times (for Saturn long-pulse mode) limit the current to near 3 MA.

In choosing the wire sizes and masses in Table 2.1, the 0D-type code was used iteratively for each shot to arrive at a wire size that met the implosion time requirement given the specified array width and wire number. Another constraint was available wire sizes in the Center 1600 inventory, which for a few shots limited the choice of array mass so that an exact match in predicted implosion time was not possible for all shots in the width scan experiment. The results of the pre-shot modeling is shown in Table 2.2. As will be seen in the section of this report discussing the experimental results, these predictive simulations did a reasonable job of accurately predicting the load current via the Saturn circuit coupling. Although the pre-shot predicted

implosion times were somewhat late, the general trends were captured. Post-shot comparison between the experimental results and the model can be used to refine the circuit parameters for better fidelity in future shot planning.

Table 2.2 also indicates the **jxB**-coupled energy for each shot simulation. This is essentially the kinetic energy of the imploding mass, as is the case in a 0D simulation of a cylindrical array, but it also includes energy that is dissipated as the wires collide sequentially during the implosion. Momentum is conserved during each collision, but energy is not and the lost kinetic energy is tracked by the code in order to quote the total coupled energy via **jxB** work at the end of the simulation. As with 0D models of cylindrical arrays, an effective final position for the implosion front must be specified at which the simulation will end and the **jxB** work will cease. In these simulations, that final value was taken as $x_f = 100~\mu$m, which is likely too small. Based on x-ray imaging that will be presented, a value of $x_f = 500~\mu$m may be more reasonable, and these calculations should be repeated to study the sensitivity of the coupled energy to x_f. For now, we can consider this to be a reasonable estimate of the coupled energy which may in fact be an upper limit. The issue of energy coupling will be discussed further in the context of post-shot simulations of experimental data presented below.

Description of x-ray diagnostics

Three lines-of-sight (LOS) were employed in the May-June 2007 Saturn planar array shot series, each at 35° from the horizontal. Views from each LOS are shown in Fig. 2.8, with the position of the pinch shown by a thin gray column on the hardware axis. These views were used to quantify and correct for the limitation in axial field of view of the stagnated plasma in analyzing the diagnostic data.

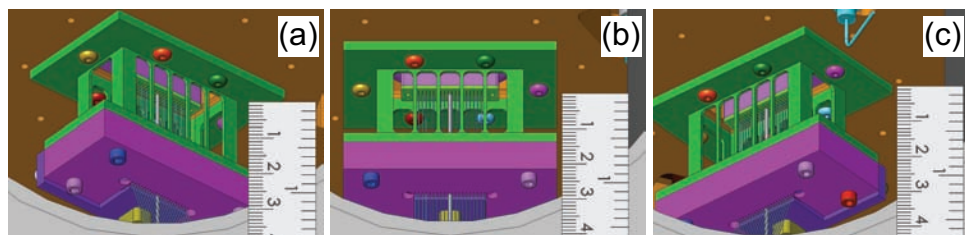LOS A and LOS B each fielded a 5 μm kimfol filtered x-ray detector (XRD) [29]

Figure 2.8. Orthographic views of the load region at 35° below the horizontal from (a) LOS A, (b) LOS B, and (c) LOS C. The z-pinch axis is indicated by a thin gray column. The rulers shown are in the plane perpendicular to the viewing line of sight. Courtesy of M. Vigil (1675).

and a bare Ni bolometer [30] to characterize the total radiated soft x-ray power and yield. The bolometer provides a measurement of total yield expected to be accurate to 15%. We follow the typical practice of normalizing the XRD waveform to the total bolometer yield in order to infer the x-ray power pulse, which is expected to be accurate to 25%. This power waveform is then integrated to infer the x-ray yield in the pre-pulse (defined as the time prior to the extrapolation of the 20-80% rise to zero), the rise up to the main x-ray peak, and the energy in the first pulse prior to the back side of the full width at half maximum (FWHM). This procedure assumes that the XRD waveform, which responds to photons in the window below the carbon edge at 284 eV, is representative of the total x-ray radiation pulse. The correspondence between the XRD and the smoothed, differentiated bolometer signal was verified on shot 3675 where the pulse was broad and fairly smooth, and such a bolometer differentiation could be reasonably carried out. There is a concern for Al loads that the K-shell photons can pass through the 5 μm kimfol filter above 1 keV and dominate the XRD signal over the photons passing through the lower transmission carbon window [31], however this is more of a concern for shots such as on Z where a very significant fraction of the total radiated power ($\sim$30%) is emitted in the Al K-shell range. A Lambertian correction for an optically thick surface radiator was performed on the bolometer yield (and thus x-ray power) data quoted, but at the 35° viewing angle this amounted to only a -5% adjustment from the calculated 4π (optically thin emission) values.

Photoconducting detectors (PCDs) [32, 33, 34] filtered with 8 μm Be + 1 μm CH were also fielded on LOS A and B to look at radiated power at photon energies > 1 keV. In the case of the Al z-pinch studied (shot 3688), these can be used quantitatively to determine the K-shell power and yield. For this analysis, it is assumed that all of the K-shell energies is emitted at the Al Ly-α photon energy (1.7 keV) for purposes of performing a filter transmission correction. This is the brightest line observed spectroscopically, and the filter transmissions are high enough at the K-shell energies ($\geq$80 %) that the resulting error due to uncertainty in the spectral shape is less than 10%. Power and yield values quoted represent the average of 4π and Lambertian-corrected values due to uncertainty in the opacity of the K-shell emission, but as noted above this is a small adjustment. We expect Al K-shell power and yield values quoted to be accurate to 25%. For tungsten pinches, whose PCD signals are smaller than for Al K-shell, the detectors are likely responding to the tail of a broad continuum, and so quantitative analysis of PCD data is not practical without detailed and accurate spectral shape characterization data which are not available. It is still useful in some cases, however, to qualitatively observe when the > 1 keV photon emission is turning on for W loads.

A pinhole camera diagnostic was also fielded on LOS B to perform 1 ns gated x-ray imaging of the planar array implosions in order to study their dynamics. As shown in Fig. 2.9, this instrument includes three 8-frame microchannel plate cameras. Two cameras (MLM1 and MLM3) view the z pinch via reflection from multilayer mirrors, which act as monochromators and reflect narrowband photons in the 100-700 eV x-
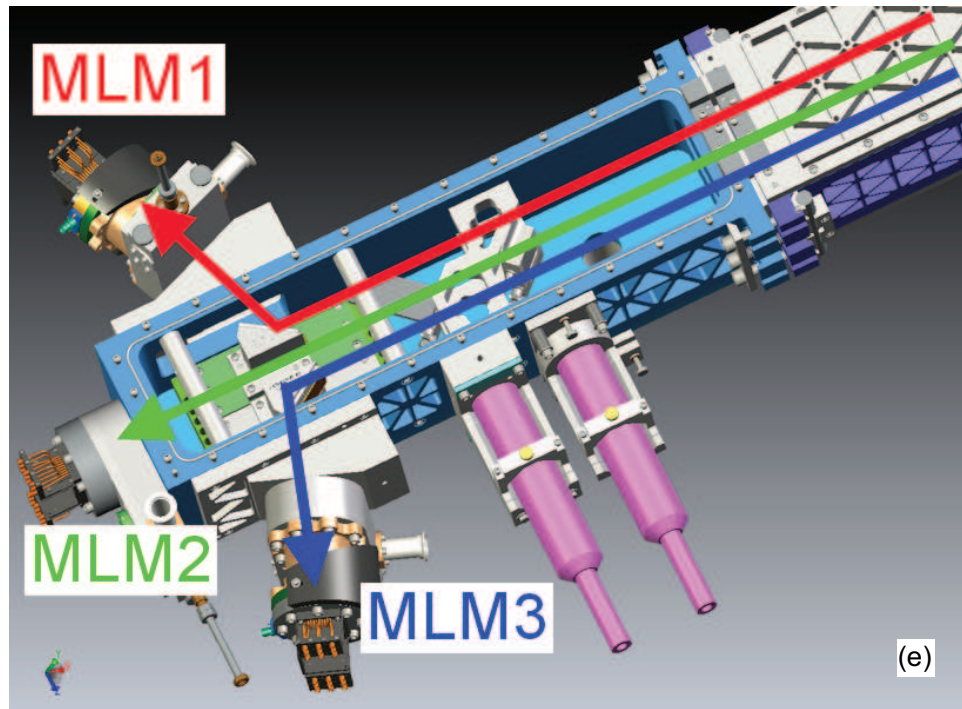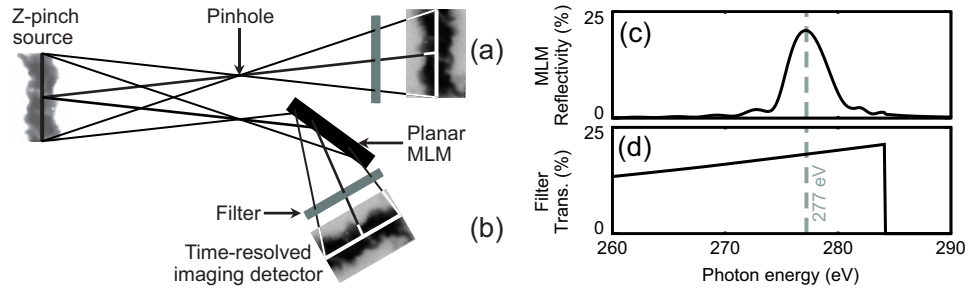
Figure 2.9. A time-resolved pinhole camera diagnostic is employed on Saturn which includes both standard filtered pinhole cameras (a) and pinhole cameras that reflect from a multilayer mirror monochromator (b). The multilayers reflect a narrow band of photons near 277 eV (c) while an aluminized kapton filter attenuates visible light and second order reflection (d). The Saturn instrument (e) combines two eight-frame 277 eV photon energy MLM cameras (MLM1, MLM3) with an eight-frame standard pinhole camera (MLM2) filtered for >1 keV photons. Figures (a-d) are reprinted with permission from B. Jones *et al.*, "Monochromatic X-Ray Self-Emission Imaging of Imploding Wire Array Z-Pinches on the Z Accelerator," IEEE T. Plasma Sci. **34**, 213 (2006), Figs. 1, 2. ©2006, IEEE.

ray range. For these experiments, two Cr/C mirrors were fielded to reflect 277 eV photons with < 10 eV bandpass as shown in Fig. 2.9(b). The third camera (labeled MLM2 but not incorporating a mirror) is a standard filtered pinhole geometry, and 8 μm Be + 1 μm CH was employed to match the PCDs and image > 1 keV photons. May-June 2007 is the first shot series for which this instrument has been fielded on Saturn, where it will remain available to support future shots on the facility. A similar version of this diagnostic has been previously fielded on the Z machine [35, 36, 37, 38] and will be available as a core diagnostic on the refurbished Z machine.

A time-integrated crystal spectrometer (TIXTL) [39, 32] was fielded on LOS C for one shot only (3688) to measure the Al and Mg K-shell lines. This instrument used a convex KAP crystal with 2 inch bending radius and 20° crystal rotation with a 0.5 mil Be filter and a 300 μm slit for one-dimensional (axial) spatial resolution of ~900 μm at 1/2 magnification. Al 5056 wires were used for this shot, which have a 5% Mg dopant content so that Mg K-shell lines are less likely to be affected by opacity than Al lines (although it is still a consideration given the relatively high mass fielded).

Electrical diagnostics on these Saturn shots included MITL B-dots and GI-type load B-dots for measuring MITL and load current. Two shots (3674 and 3685) fielded a voltage monitor probe that inductively coupled the cathode above the load to the MITL wall across the convolute in order to measure the voltage and inductance of the load [40]. The installation of this monitor had to be performed after the wire array load was installed as it was designed to attach to the retaining nut above the load cathode. This led to a disturbance of the load and MITL regions as the diagnostician was required to stand on the MITLs and mount to the hardware feature that was holding the wire array in place. As a result, it was noticed post-shot on 3674 that wires had been broken during this pre-shot alignment (untarnished weights were found lying on the bottom lid after breaking vacuum), and so data from that shot is unusable. This problem did not reoccur on shot 3685, but on both shots the MITL current was higher than usual and the load current and x-ray output were low. We believe that the MITL was misaligned while it was being walked on, causing a post-hole convolute short. Thus, the data from 3685 cannot be used as part of a width scaling scan, however the load current and x-ray measurements are valid and this shot stands on its own for investigation of planar array dynamics and current scaling. This is important because it is the only tungsten wire array fielded for which the MLM imager was timed early enough to observe the implosion of the planar wire array during the rise of the main x-ray pulse. Images of the implosion were also obtained on 3688, the Al 5056 planar array.

Two diagnostic timing problems were discovered during this shot series. One was a ~30 ns error in the MLM imager frame timing due to an error in the header file. This resulted in images being recorded later than we had thought, thus most of the images obtained were after peak x-ray power. A ~5 ns timing shift was found for the LOS A and LOS B bolometers by comparing to a machine B-dot reference signal in that screen box. M. A. Torres (1342) noted the error and corrected the header to account

for it, and is continuing to track down the source of the discrepancy. Both of these errors will be eliminated in future shots, and can be corrected for post-shot for the May-June 2007 Saturn shots. Timing is expected to be accurate to 1 ns on Saturn.

Chapter 3

Discussion of Experimental Results

As discussed above, shots 3670, 3671, 3672, 3675, and 3682 constitute a mass and implosion time scan, while shots 3670, 3682, 3683, 3684, and 3686 comprise a width scan for planar arrays from the May-June 2007 Saturn shot series. Shot 3674 suffered from a post-hole convolute short as well as broken wires and so is unusable. Shot 3685 also appeared to suffer a post-hole convolute short and lower load current and so cannot be included in the width scan, however we will include this shot in a current scaling comparison and will use imaging data to address planar array dynamics. For shot 3673, we attempted to shoot a second shot in a single day by leaving the MITLs in place and not refurbishing them. This shot produced comparable current and yield to shot 3672, which was otherwise identical, however the x-ray pulse shape was changed and the power reduced. We have elected not to include this shot in the scaling studies as there is residual concern regarding whether the dirty MITLs could have somehow impacted the wire array performance.

Table 3.1 shows measured load current, implosion time, x-ray rise time and FWHM (for both LOS A and B XRD measurements) for all of the planar array shots. Tables 3.2 and 3.3 indicate the measured x-ray yields in the prepulse, rise to peak, main pulse, and total pulse for LOS A and B respectively. These tables also indicate the calculated coupled energy estimated with the 0D-type code described above which was in this case run post-shot using measured load current waveforms rather than including the Saturn circuit model. We consider this to be our most reliable estimate of **jxB** input energy for each shot, although note the concern mentioned above regarding the choice of final stagnation position in the model. In the following sections we will plot and make reference to these data, but they are included in tabular form here for completeness in this report.

We note that the implosion times listed in Tables 3.2 and 3.3 are somewhat shorter than the pre-shot predictions in Table 2.2. This is fortunate in some sense, as the measured current levels were in the $\sim$3 MA range as predicted, but the nominal implosion time is near 100 ns, in the correct range for comparison with Zebra and Z generators. The discrepancy is something to be considered, though, and we discuss this further in the section on planar array dynamics.

Table 3.1. Experimental data for the Saturn shots described in Table 2.1, including load current from B-dot diagnostics and x-ray pulse timing from XRDs on LOS A and B. Implosion time is defined as the time of peak total x-ray power relative to the extrapolation to zero of the linear rise of the load current (45-70% of peak current or 4 MA for shot 3675).

^{m}Shots used in mass (implosion time) scan.
^{w}Shots used in width scan.
^{i}Shots used for current scan with Zebra data in Table 3.4.
*Voltage monitor was fielded, but reduced load current perhaps due to post-hole convolute short was observed.
†Wires broken pre-shot; data are not usable.
‡MITLs not pulled and cleaned prior to shot; data may or may not be usable.

Shot number	Peak current (MA)	LOS A			LOS B		
		Implosion time (ns)	10-90% rise time (ns)	FWHM (ns)	Implosion time (ns)	10-90% rise time (ns)	FWHM (ns)
3670^{mw}	2.8	96.0	16.6	16.7	96.0	19.3	15.4
3671^{m}	2.4	81.4	20.6	25.7	92.2	28.4	12.3
3672^{m}	3.6	101.1	9.2	8.0	100.9	8.4	6.4
$3673^{\ddagger}$	3.4	110.6	22.6	25.4	110.4	24.6	25.2
$3674^{*\dagger}$	2.1	109.7	20.0	19.5	104.7	34.2	25.9
3675^{m}	6.0	175.5	35.1	24.2	175.5	26.2	31.0
3682^{mw}	3.0	91.2	11.3	16.1	91.0	12.5	17.1
3683^{wi}	3.2	99.4	18.2	13.5	94.4	14.8	17.5
3684^{wi}	3.0	94.8	13.8	13.8	93.4	13.2	13.0
3685^{*i}	2.6	103.5	19.4	19.6	103.3	18.8	19.7
3686^{wi}	2.6	90.9	12.7	13.8	90.7	14.8	15.1
3688	3.6	90.4	15.3	19.5	90.0	12.9	19.3

Table 3.2. Experimental total radiated x-ray power and yield data from diagnostics on LOS A for the Saturn shots described in Table 2.1. Calculated coupled energy is from 0D-type modeling using the measured current waveform and assuming $x_f = 100\mu m$ (courtesy of A. A. Esaulov, University of Nevada, Reno).

^{m}Shots used in mass (implosion time) scan.
^{w}Shots used in width scan.
^{i}Shots used for current scan with Zebra data in Table 3.4.
*Voltage monitor was fielded, but reduced load current perhaps due to post-hole convolute short was observed.
†Wires broken pre-shot; data are not usable.
‡MITLs not pulled and cleaned prior to shot; data may or may not be usable.

Shot number	Peak power (TW)	Yield in prepulse (kJ)	Yield to peak power (kJ)	Peak power $\times$FWHM (kJ)	Yield to back of FWHM (kJ)	Total yield (kJ)	Calculated coupled energy (kJ)
3670^{mw}	11.9	14.1	99.3	197.6	197.9	282.2	66
3671^{m}	6.3	6.6	69.3	162.6	143.1	175.8	46
3672^{m}	12.2	15.9	59.5	97.9	113.8	281.6	113
$3673^{\ddagger}$	7.8	14.2	122.6	199.1	203.6	273.0	113
$3674^{*\dagger}$	3.6	7.7	52.9	69.4	73.2	92.4	NA
3675^{m}	7.6	21.3	118.3	183.6	198.3	304.5	288
3682^{mw}	8.7	10.4	52.5	140.3	126.0	177.0	74
3683^{wi}	4.6	9.2	43.1	62.1	63.4	152.3	63
3684^{wi}	7.1	11.0	58.7	97.8	101.0	167.1	64
3685^{*i}	3.9	6.7	36.3	75.9	77.9	106.0	47
3686^{wi}	5.8	6.7	44.1	80.6	74.3	186.7	46
3688	5.5	7.8	47.4	106.8	104.6	215.0	109

Table 3.3. Experimental total radiated x-ray power and yield data from diagnostics on LOS B for the Saturn shots described in Table 2.1. Calculated coupled energy is from 0D-type modeling using the measured current waveform and assuming $x_f = 100\mu m$ (courtesy of A. A. Esaulov, University of Nevada, Reno).

^{m}Shots used in mass (implosion time) scan.
^{w}Shots used in width scan.
^{i}Shots used for current scan with Zebra data in Table 3.4.
*Voltage monitor was fielded, but reduced load current perhaps due to post-hole convolute short was observed.
†Wires broken pre-shot; data are not usable.
‡MITLs not pulled and cleaned prior to shot; data may or may not be usable.

Shot number	Peak power (TW)	Yield in prepulse (kJ)	Yield to peak power (kJ)	Peak power ×FWHM (kJ)	Yield to back of FWHM (kJ)	Total yield (kJ)	Calculated coupled energy (kJ)
3670^{mw}	11.7	25.7	77.8	180.6	160.4	306.7	66
3671^{m}	9.2	3.0	120.3	113.2	139.0	195.8	46
3672^{m}	11.3	17.7	56.3	72.3	89.0	315.3	113
$3673^{\ddagger}$	7.7	16.0	116.0	195.1	191.9	305.0	113
$3674^{*\dagger}$	2.9	8.7	32.9	76.1	68.3	113.1	NA
3675^{m}	8.4	28.0	123.7	259.7	242.8	426.9	288
3682^{mw}	8.4	13.9	51.9	144.2	133.6	218.1	74
3683^{wi}	4.3	9.7	31.3	75.6	74.0	201.3	63
3684^{wi}	8.1	11.4	61.1	105.6	112.0	224.3	64
3685^{*i}	3.9	7.5	36.7	77.4	77.1	133.6	47
3686^{wi}	5.0	9.0	42.9	75.0	70.3	232.1	46
3688	4.7	7.0	38.3	89.9	83.0	267.5	109

Tungsten planar wire array total radiated power scaling

Figure 3.1 shows total radiated power, 10-90% rise time, FWHM, and yield over various ranges of the x-ray pulse for the mass scan data set. From Fig. 3.1(a-b), the optimal mass for x-ray power generation using this load hardware style appears to be ~1 mg/cm, although the limited number of data points and the shot-to-shot variation observed in the twice-repeated experiment at 0.5 mg/cm make it difficult to be precise. The highest power shot was at 12 TW, though to be conservative given the apparent shot-to-shot variation we quote 10±2 TW as the optimal power obtained with these 3 MA planar wire arrays at 20 mm width and 100 ns implosion time. It is clear that for the shortest implosion time studied (~85 ns, 0.248 mg/cm, shot 3671) the yield was reduced and the rise-time increased. For the longest implosion time and highest mass case (175 ns, 3.957 mg/cm, shot 3675) the yield has actually increased beyond any of the shorter implosion time shots, although the rise-time and FWHM have also increased, resulting in a drop in the peak x-ray power.

From Fig. 3.1(c), we see that the 0D-calculated coupled energy increases with mass and implosion time, which makes sense as the peak load current is also increasing. We can make the nominal statement that the calculated **jxB**-coupled energy explains the yield in the first x-ray pulse. It is clear that our optimistic estimation of **jxB** input energy does not explain the total x-ray yield. This is not particularly surprising; the same observation has been previously made for cylindrical wire array implosions [41, 42], with proposed explanations including additional plasma compression and PdV work post-stagnation [43], m=0 [44, 45, 46] or m=1 [10] instabilities enhancing resistive or inductive energy deposition, and Hall effect enhancements in Ohmic heating [9]. It is interesting that the calculated coupled energy comes close to explaining the total yield for the highest mass case, while it does not even explain the yield to peak x-rays for the lightest load. This could indicate that resistive heating (or whatever energy coupling mechanism is at work) can play a more or less significant role in the overall energy balance depending on the location in parameter space of a particular load design. The data do not exclude the possibility that a possible Ohmic mechanism deposits a fixed amount of energy in the z pinch for all masses studied in addition to the kinetic energy coupled (which increases with mass). Finally, we note that there appears to be a systematic trend in comparing data from LOS A and B (on which independent bolometers and XRDs were fielded): they agree well in the in first x-ray power pulse, but LOS B repeatedly shows a higher total x-ray yield due to an enhanced tail of the x-ray pulse. This could indicate that opacity is playing a role in limiting the late-time power from LOS A, which views the pinch at an angle to the array plane normal direction. We do not have imaging on LOS A, though, so we can't exclude the possibility of one of the return current cage bars occluding some of the omission from the broader plasma column that is seen after the x-ray peak (to be discussed in the following section on implosion dynamics).
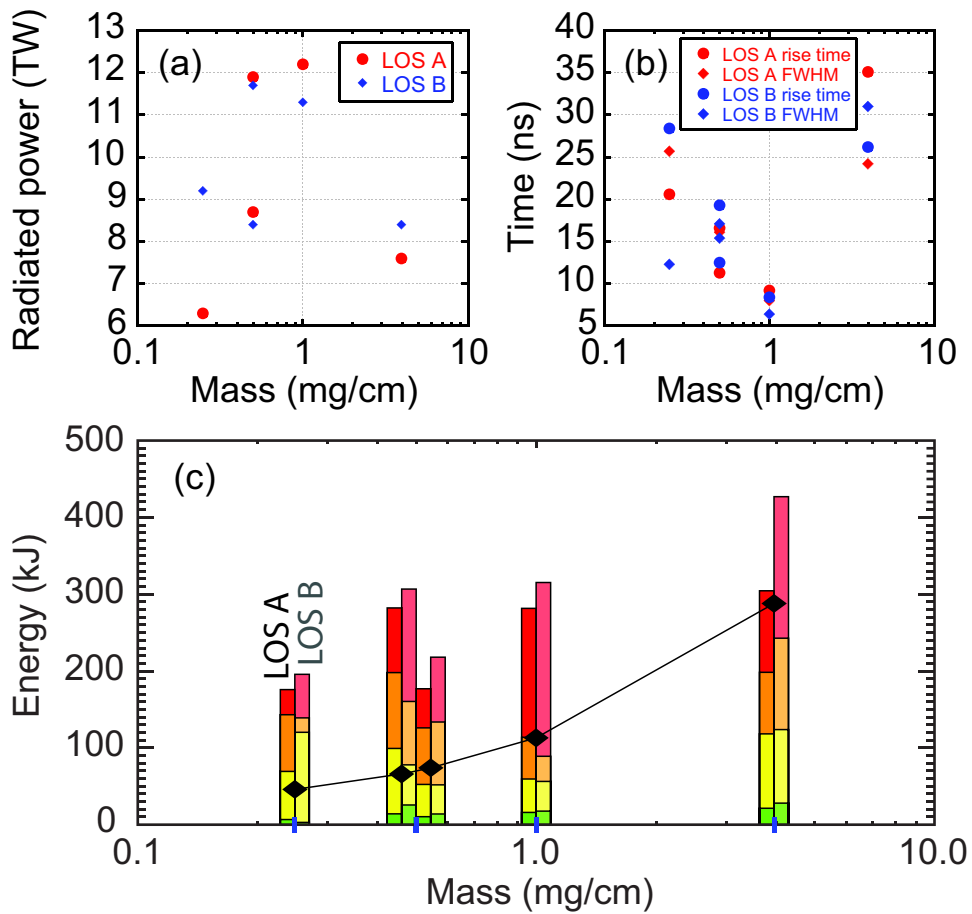
Figure 3.1. Mass (and implosion time) scan scaling results for shots 3670, 3671, 3672, 3675, and 3682: (a) Total radiated power, (b) 10-90% rise time and FWHM, and (c) radiated soft x-ray yields. The tops of the colored bars indicate total yield (red), yield to the back of the FWHM (orange), yield to peak (yellow), and pre-pulse yield (green). The four masses fielded are indicated by blue tick marks (the bars are offset from these points for clarity). Data from LOS A and B diagnostics are shown for each shot, with LOS B in paler colors. Coupled energy calculated in the 0D-type model using measured current waveforms and assuming x_f=100 μm is shown (black diamonds).
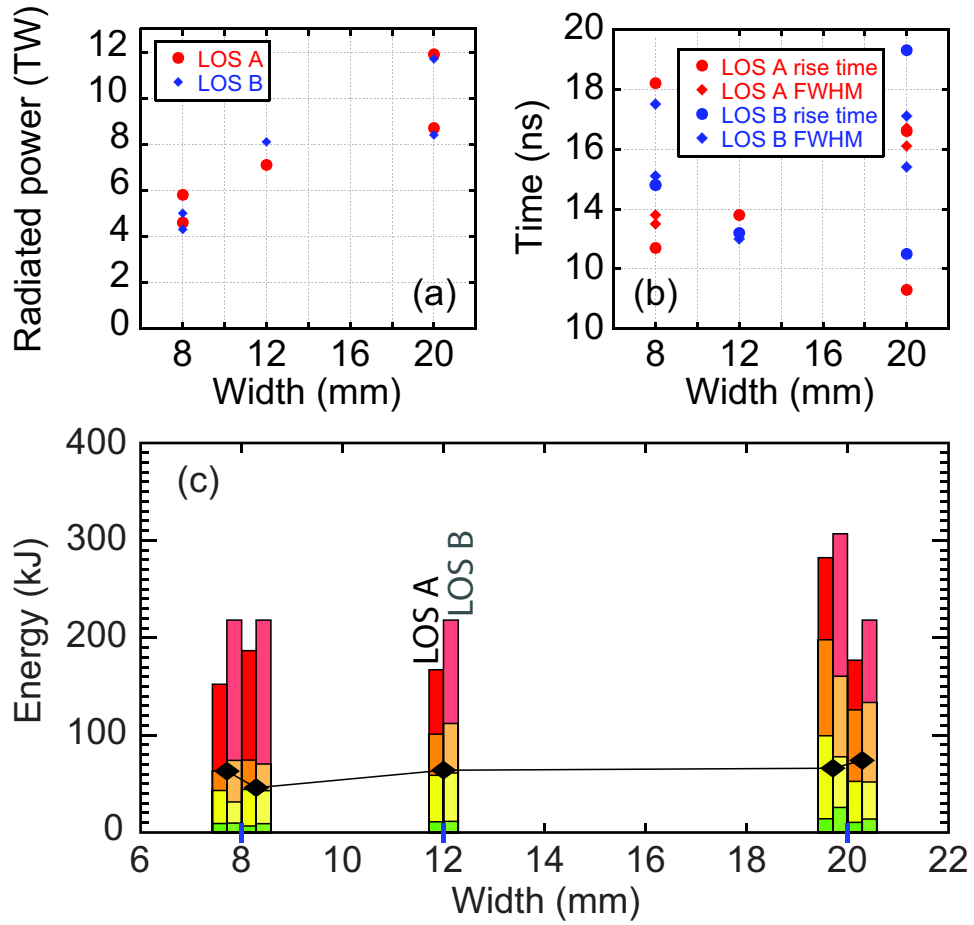
Figure 3.2. Width scan scaling results for shots 3670, 3682, 3683, 3684, and 3686: (a) Total radiated power, (b) 10-90% rise time and FWHM, and (c) radiated soft x-ray yields. The tops of the colored bars indicate total yield (red), yield to the back of the FWHM (orange), yield to peak (yellow), and pre-pulse yield (green). The three array widths fielded are indicated by blue tick marks (the bars are offset from these points for clarity). Data from LOS A and B diagnostics are shown for each shot, with LOS B in paler colors. Coupled energy calculated in the 0D-type model using measured current waveforms and assuming x_f=100 μm is shown (black diamonds).

Figure 3.2 shows the same quantities as Fig. 3.1, but for the planar array data set encompassing a width scan at approximately constant implosion time (∼95 ns). The total radiated power is seen to drop with reduced array width. One presumes this trend would hold in a planar-z-pinch-driven ICF scheme, however the primary hohlraum surface area would also drop with reduced array initial width. As mentioned earlier, an integrated hohlraum/pinch energetics study is required to determine the optimum load and hohlraum geometry. The shots at 8 mm and 20 mm width were each reproduced twice, with a fair amount of shot-to-shot variation seen in Fig. 3.2(b). The comparison of measured yields and calculated coupled energy in Fig. 3.2(c) suggests that the **jxB**-coupled energy can explain the yield to peak x-ray power, but not the total x-ray yield. We note that the 0D-type modeling indicates little variation in coupled energy with array width (contrary to initial analytic expectations [6]), while the experiment does show somewhat of a drop in yield at smaller initial array widths. Comparing the three plots in this figure, it is seen that the trend in power reduction at small widths is due to the drop in yield in the first x-ray pulse, and not due to any strong trend in pulse shape.

These data could serve to test various hypotheses about energy coupling, including Hall resistivity which A. S. Chuvatin (Ecole Polytechnique) and L. I. Rudakov (Icarus Research) may continue to address in future theoretical/numerical work, but we are not able to resolve the question based on these experiments alone. The strongest statement we can make here is that the **jxB**-coupled energy may explain approximately the energy in the first x-ray pulse, but it cannot explain the total x-ray yield. We are not able to say at present at what stage in the pinch evolution resistivity may become an important energy deposition channel, though we continue to discuss these issues in the following section.

A final desirable scaling assessment is the dependence of peak radiated x-ray power on the peak load current. An observed strong dependence would imply favorable results for planar arrays when scaled to current levels typical of the Z machine. Experiments on the Zebra generator [47] were planned in collaboration with and conducted by V. L. Kantsyrev (University of Nevada, Reno) as indicated in Table 3.4. The goal was to match array width, wire number, and implosion time as closely as possible to the Saturn loads discussed above, and use the resulting 1 MA shots to compare the peak x-ray power to the 3 MA Saturn shots. These experiments were constrained by the smallest sizes of available tungsten wire; 20 mm wide arrays were not fielded on Zebra as the required wire size would have been impractical, but 8 mm and 12 mm were possible. One caveat to these experiments is that the machine return current geometry and thus load inductance was significantly larger on Zebra; we need to address whether this impacted the calculated coupled energy for these loads. Another caveat is that the Zebra implosion times were slightly longer (with noticeable shot-to-shot variation on both drivers) and the current pulse shape not identical; we have not attempted to correct for these issues in the present comparison.

Even with these caveats, it is still interesting to take an initial look at planar array

Table 3.4. Planar wire array experiments on the Zebra generator with approximately matched width, wire number, and implosion time for power scaling comparison with Saturn loads. All arrays are tungsten with 20 mm height. Courtesy of V. L. Kantsyrev (University of Nevada, Reno).

Shot number	Array width, W (mm)	Wire number	Wire diameter (μm)	Array mass (mg/cm)	Implosion time (ns)	Peak load current (MA)	Peak power (TW)
1249	11.5	24	5	0.091	110	0.80	0.58
1250	11.5	24	5	0.091	110	0.82	0.57
1251	7.5	16	8.9	0.192	105	0.88	0.48
1252	7.5	16	8.9	0.192	125	0.88	0.49

power scaling from 1 MA to multi-MA z pinches. Figure 3.3 shows the Zebra data from Table 3.4 along with the Saturn shots of 8 mm (3683, 3686) and 12 mm (3684, 3685) width. We note that 3685 suffered a convolute short and was not a true repeat of 3684, however the load current and x-ray power measurements are valid and we expect that it is fair to include this point in a current scaling plot. The Saturn peak x-ray powers from LOS B are shown here, chosen over LOS A due to the previously mentioned concerns about the oblique view of the stagnated pinch. Linear least-squares fits to log(Power) vs. log(Current) were performed to determine the scaling exponent, which is close to $P \propto I^2$ for both the 8 mm and 12 mm cases. As shown in Fig. 3.3, best fit values indicate $P \propto I^{1.9\pm0.2}$ for both the 8 mm and 12 mm widths.

This I^2 power scaling is expected in the ideal case for any geometry z-pinch load when the implosion dynamics are self-similar as generator current is scaled up. That is, the coupled energy and thus x-ray yield is expected to scale as I^2, and so if the implosion follows the same trajectory with the same basic physics determining the x-ray production and the x-ray pulse shape remaining the same, then the peak power will also scale as I^2. In reality, other physics concerns such as the role of wire ablation, instability growth, and scaling of plasma heating mechanisms make the picture significantly more complicated, and a consensus is still lacking as to how cylindrical wire array total power scales with generator current [21, 48, 49]. Some of the same scaling arguments in the cited works may be applied to the present planar array data, but it is also extremely desirable to obtain data at more than just two current levels. If we take the present preliminary result at face value and scale 10 TW at 3 MA up to 20 MA assuming $P \propto I^2$, for example, we obtain over 400 TW which seems dubious. It is premature, based on the data discussed here, to assume $P \propto I^2$ scaling to the multi-MA range beyond the present data set. Optimum planar array mass on Saturn at 3 MA is similar to optimum cylindrical array mass on Z at 10-15 MA; wire ablation effects may dominate as planar arrays are scaled upwards toward 6-25 MA. We plan to conduct follow-on Saturn experiments at the ~6 MA
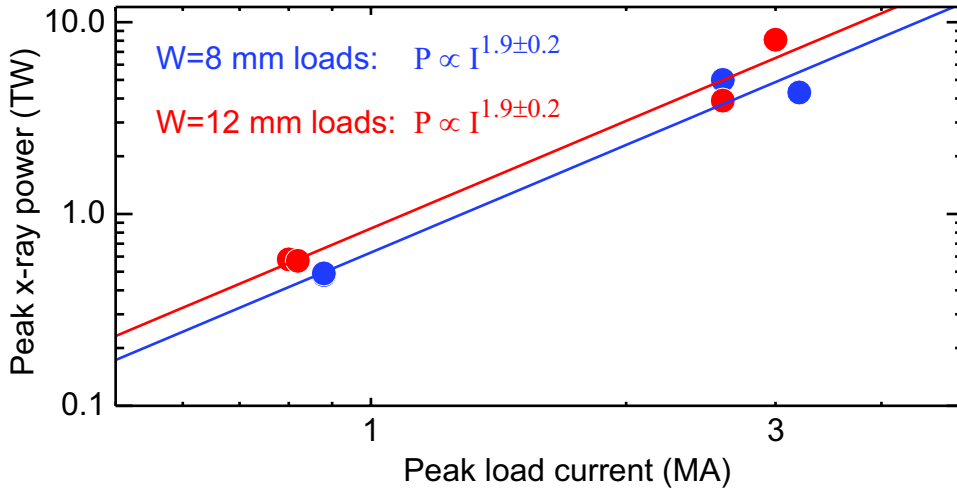
Figure 3.3. X-ray peak power scaling with peak load current from Zebra experiments in Table 3.4 and Saturn shots 3683, 3686 (8 mm width) and 3684, 3685 (12 mm width). X-ray power appears to scale favorably as I^2, however the data is sparse and higher-current data are required to establish greater relevance to potential Z experiments. Zebra data courtesy of V. L. Kantsyrev (University of Nevada, Reno).

current level, which would start to become more relevant to ICF schemes that one could envision for the Z machine using planar wire arrays. It would also, of course, be desirable to understand the implosion dynamics and energy coupling mechanisms relevant to planar wire arrays in order to motivate the observed power scaling based on physics principles. This is a difficult task for any z-pinch geometry, and we start to address this in the following section.

Planar wire array implosion dynamics

Figure 3.4 shows current and x-ray power data for shot 3672, which we will discuss here as an example of the post-shot analysis using the 0D-type modeling. For many of these shots, it is found that even using the measured load current waveform in the simulation, the implosion time is still too late relative to the measured x-ray power pulse. This is apparent for the coupled energy bar labeled $m_L/I^2 = 100\%$, in which the simulation was performed assuming 100% mass participation in the implosion front. Agreement with the measured time of peak x-rays can be obtained by using only 50% of the initial array mass in the simulation. This can be interpreted as evidence that significant mass ($\sim 50\%$) trails the leading implosion front due to magnetic Rayleigh-Taylor-type instability. A qualitatively similar conclusion has been
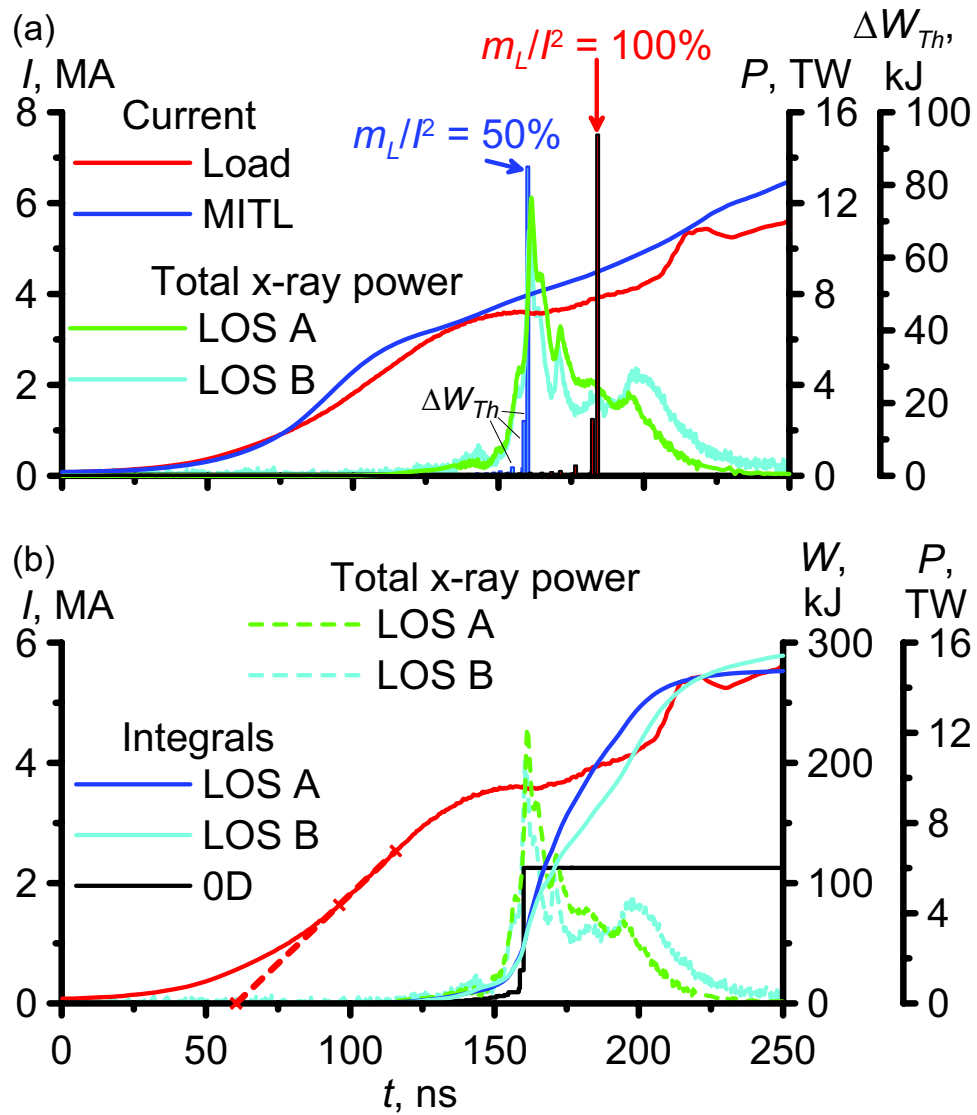
Figure 3.4. Post-shot modeling of the experiment using the measured load current waveform for shot 3672. Measured total radiated x-ray power is shown for each line of sight along with measured MITL and load currents. The time base is relative to the start of the open circuit voltage waveform. (a) The calculated implosion time with 100% mass participation is later than the experiment; reducing the implosion front mass by 50% provides better agreement. Calculated coupled energy ΔW_{Th} varies little between these two cases. (b) Integrated calculated 0D yield is shown along with integrated experimental yield for each LOS. Calculated input energy may explain the first x-ray pulse but not the total measured yield. The dashed red line shows an extrapolation of the linear load current rise to define t=0 for referencing the implosion time. Courtesy of A. A. Esaulov (University of Nevada, Reno).

reached for cylindrical wire arrays at 1-20 MA [50, 51, 40], where it was concluded that 30-50% of the mass may trail behind the fastest implosion front at the foot of the power pulse.

In Fig. 3.4(a), the total calculated coupled energy is the sum of the series of bars each of which indicates the energy ΔW_{Th} thermalized at each collision between adjacent wires. We note that these values are very similar for the 50% and 100% mass participation cases, indicating that our 0D-type estimate of the coupled energy is not terribly sensitive to the mass fraction participating in the implosion and stagnation. We also note, though, that the total coupled energy is dominated by the final collision, and the value for this last ΔW_{Th} bar will be sensitive to the final wire position assumed in the calculation, as discussed previously. Figure 3.4(b) shows the summed coupled energies as the black curve labeled "0D" along with the integrated x-ray waveforms, showing the instantaneous yield. Comparing these along with the x-ray power pulses, we see that the code calculation of coupled $\mathbf{j} \mathbf{x} \mathbf{B}$ energy may explain at most the yield in the first x-ray pulse, but certainly not the total yield.

The time base in Fig. 3.4 is relative to the start of the open circuit voltage waveform used in the simulation. The figure also shows a linear fit to the 45-70% rise of the measured load current, capturing the linear rise stage of the current waveform. The extrapolation of this line to zero current gives the t=0 point for purposes of defining the implosion time (the time of peak x-ray power) in Table 3.1. The same procedure was applied to modeled load currents in defining the implosion times in Table 2.2 and in the post-shot simulations.

Soft x-ray self-emission imaging data at 277 eV photon energy are shown in Fig. 3.5 from shot 3685, which is the one tungsten shot where we were successful in obtaining images of the implosion prior to peak x-ray power. We must qualify the analysis of these images in that the x-ray self-emission is a function of density as well as temperature, and so inferences about the mass profile evolution can be impacted by the temperature evolution. A clear edge to the implosion front is seen in part (a), although there is axial variation including bright spots at several locations along the dimmer emission filling the interior volume. The bright spots and the edge of the dimmer emission do appear to be aligned, though. In the following we assume that this implosion front represents the leading edge of the imploding mass, i.e. the magnetic-Rayleigh-Taylor-induced bubbles which in cylindrical arrays are believed to deliver significant mass and kinetic energy to the axis [52]. Fig. 3.5(b) shows line-outs across each of these images, averaging over the full axial height of the image. An implosion front is seen, along with emission on axis at early times which likely indicates the presence of a precursor plasma column (dim, but also seen in the images). To quantify the implosion trajectory, we fit a function of the form

$$I(x) = A + Be^{-\frac{(x-C-D)}{E^2}} + Be^{-\frac{(x-C+D)}{E^2}} + Fe^{-\frac{(x-C)}{G^2}} \tag{3.1}$$

to the line-out intensity $I(x)$ for each frame, where A-G are non-linear least-squares

44
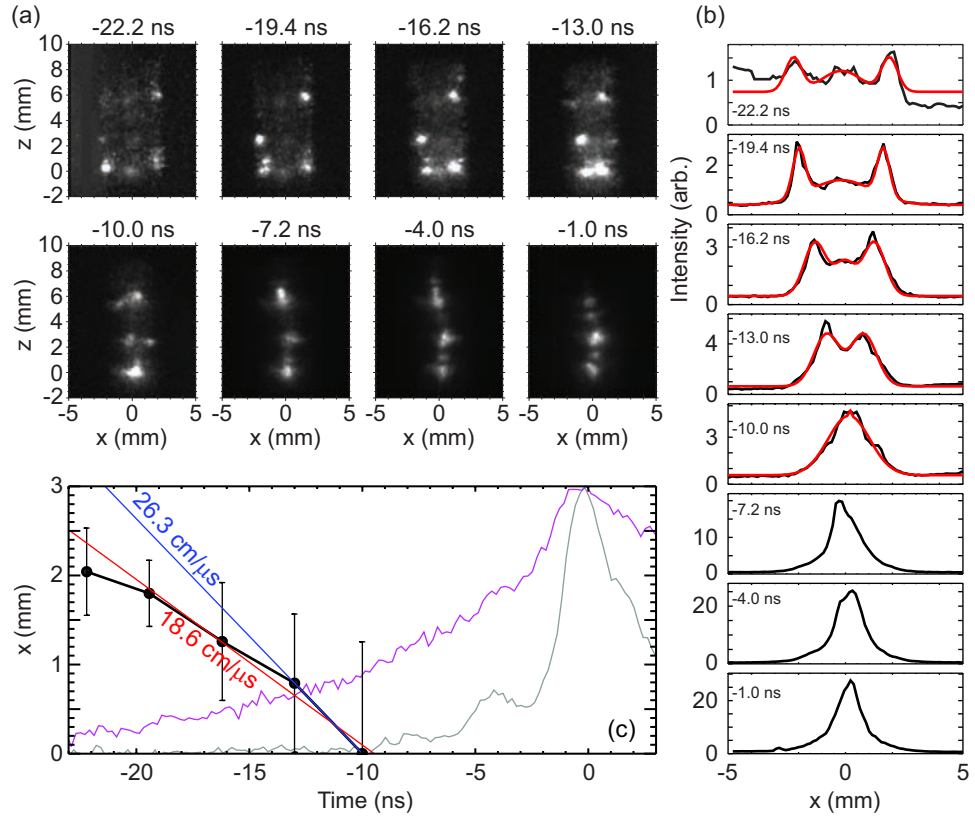
Figure 3.5. (a) Soft x-ray 277 eV self-emission images from shot 3685, MLM1 frames 1-8. (b) Line-outs averaging over axial structure in the images of part (a). Red curves show fits of Eq. 3.1 to characterize the implosion trajectory. (c) The implosion trajectory from the fits in part (b) are shown (black circles) with error bars indicating the fit width of the implosion front. Linear fits to the last four points (red) and to the last two points (blue) give a range for inferred implosion velocity. Total power (magenta) and > 1 keV PCD signals (gray) from LOS B are shown normalized.

fit parameters. These fits are indicated by red curves in Fig. 3.5(b). The first two Gaussian terms represent the implosion front, with D giving the trajectory and E the width. The last Gaussian fits the on-axis emission peak and is included to help the fidelity of the fit for the implosion front trajectory. This trajectory, inferred from the fit parameter D from each frame, is shown in Fig. 3.5(c). The error bars shown represent the width from fit parameter E, taken to be indicative of the spread in the emission front due to axial structure such as unaligned bright spots. The fit error in the trajectory is essentially negligible in comparison to the parameter E.

Viewing the trajectory by eye, it appears to be accelerating through stagnation, however given the assigned error bars it is difficult to draw this conclusion quantitatively. If we expect the trajectory to be accelerating, then we might draw a line through the last two point as indicated in blue to obtain an estimate of 26.3 cm/μs for the final implosion velocity. One might argue that we really do not know what the current convergence is in the experiment, and thus at what radius the acceleration stops. This fit uses a final point near zero, and so may reasonably be taken as an upper bound on the velocity of the implosion front. If the plasma is not accelerating in the final stage of implosion (i.e. due to the snowplow of mass or the back pressure caused by internal energy of plasma on axis) then we might instead fit a line to the last four points (shown in red) which gives 18.6$\pm$1.8 cm/μs. This can be interpreted as a lower bound on the final implosion velocity. If we assume that all of the initial wire mass is participating in the implosion, then we can estimate the coupled kinetic energy to be in the range 46-93 kJ corresponding to these two limiting velocities. If only 50% of the mass is participating in the implosion as discussed above, then the kinetic energy would be halved and so 23-93 kJ is a reasonable range to consider. From Table 3.3 (LOS B), we note that the measured pre-pulse yield was 7.5 kJ, the yield to peak power was 37 kJ, the yield to the back of the FWHM was 77 kJ, the total yield was 134 kJ, and the calculated coupled energy was 47 kJ. This analysis points again to the coupled kinetic energy explaining the energy radiated through peak x-rays or perhaps in the first pulse, but not the total radiated yield.

This discussion also illustrates the difficulty in obtaining a high-quality, reliable estimate of plasma kinetic energy. Determination of the implosion velocity is somewhat ambiguous given finite time resolution of the data and uncertainty about acceleration in the final stage of the implosion. Quantitative determination of the mass participating in the implosion is also required. Multi-frame radiography coupled with a continuity equation analysis approach [36, 53] may be a promising technique, and could be applied to quasi-one-dimensional planar array implosions as well as cylindrical geometries.

One other caveat to note is that any mass trailing the main implosion front (which must be cold and thus invisible in the self-emission images of Fig. 3.5) may continue to accelerate after the main implosion front collides on axis, as discussed for cylindrical wire arrays in Ref. [10]. Thus, the total coupled kinetic energy may be greater than the peak instantaneous kinetic energy at the start of the main x-ray pulse. The total
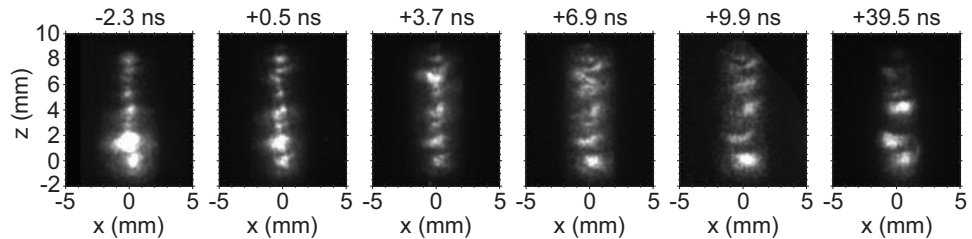
Figure 3.6. Soft x-ray 277 eV self-emission images from shot 3683, MLM1 frames 1-5 and MLM3 frame 8. The narrow 1 mm diameter pinch at peak x-rays develops in < 10 ns into a 2-3 mm column with striations that remain fairly static for tens of ns during the tail of the x-ray pulse.

x-ray power pulse and a > 1 keV PCD signal (both normalized to the plot) are both shown in Fig. 3.5(c). The start of the > 1 keV signal corresponds to the arrival of the implosion front, suggesting that on-axis heating is beginning at that time. We note that the implosion appears to stagnate approximately 10 ns before the peak x-ray power. It seems unlikely that the collisional thermalization time would be this long in a load of this high of a mass, so this may indicate that indeed trailing mass is continuing to arrive on axis during this period. This mass could be accelerating and depositing additional kinetic energy, or perhaps the dominant heating mechanism could be Ohmic, which may only become significant when the trailing mass brings the current to the axis at a time near peak x-rays.

Shot 3685 was also the one shot where we believe we may have obtained useable data with the voltage monitor. An analysis of these data is proceeding [E. M. Waisman (1673)] which we hope will be valuable in understanding the planar array dynamics. Inferred load inductance versus time would allow us to constrain the energy coupled via **jxB** in the simulations, along with the location of the current and coupled energy in the experiment. Any future shots on the Z machine for which x-ray radiography with the Z-Beamlet Laser [54] is possible would also be valuable for quantitative diagnosis of the mass distribution, including assessment of trailing mass.

X-ray imaging data from shot 3683 is shown in Fig. 3.6 to illustrate the behavior typical of these planar arrays after the peak of the x-ray pulse. A narrow 1 mm FWHM column is seen at the time of peak x-ray power with axial structure on the scale of $\sim$1 mm. Within 10 ns after the peak, this column has grown to 2-3 mm FWHM, with noticeable axial striations with a few-mm period. This structure then remains quite static for tens of ns after peak power, during the long tail of x-ray emission typical of these pinches (see Fig. 3.4, for example). From the frame at +6.9 ns, it is tempting to suggest that the initially narrow column is breaking up via m=1 MHD instability to form the broader column with longer wavelength striations. This is not conclusive from this one shot, however. Another possibility is that trailing mass is accreting on

47

the axis for $\sim$10 ns after peak x-ray power, causing the size of the pinch to grow. This could likely be addressed by studying Al planar arrays with time-resolved (and possibly radially-resolved) K-shell spectroscopy; collisional-radiative modeling of the spectra with the added constraint of measured K-shell power may reveal the amount of mass participating in x-ray emission on axis as a function of time.

It is clear from Figs. 3.5 and 3.6 that significant axial structure exists at all stages during the plasma stagnation. Although these are self-emission images which may depend on both temperature and density, it is reasonable to conclude that there is likely a density variation along the pinch length as required for Hall resistivity to begin to play a role in Ohmic heating [9, 6]. We cannot presently quantify a density contrast parameter from the experimental data, however, and so any modeling of these experiments will have to treat that as a free parameter adjusted to fit the x-ray power and yield data. While it will be interesting to see if the experimental trends can be reproduced, this is not entirely satisfactory as curve-fitting to an unmeasurable parameter does not provide strong validation of a proposed physical model. It may be possible in future experiments to measure density variation along the z-axis via spectroscopic means, through analysis of the MLM images coupled with collisional-radiative simulations following the discussion of Ref. [38], or through radiography on Z [54].

Aluminum K-shell radiation from a planar wire array

One shot (3688) used Al 5056 wires in a planar array configuration in order to provide limited initial data regarding the suitability of planar array geometries for K-shell production. As discussed previously, it is not obvious that planar arrays should work well for this application, as K-shell excitation typically requires large initial cylindrical array diameters, high velocities, and high coupled energy per ion to achieve high plasma temperatures–the mass distributed internal to a planar array near the axis seems to work against this goal.

Figure 3.7 shows the LOS A and LOS B K-shell power measured by PCDs, along with normalized XRD signals for pulse shape comparison. The total Al K-shell yield was about 10 kJ at a load current of 3.6 MA (Table 3.1). This yield is not particularly attractive at first glance; we note that $\sim$25 mm diameter cylindrical Al wire arrays on Saturn have produced 60-90 kJ of K-shell x-rays at 8 MA in previous experiments [5]. Assuming an I^2 scaling in yield, however, the 10 kJ yield would scale up to 50 kJ at 8 MA. A planar array might actually be competitive with cylindrical arrays if load hardware could be designed to achieve that current level with a planar wire array. The 10 kJ of Al K-shell from shot 3688 is a fairly small fraction of the 268 kJ (Table 3.3) total x-ray yield for this shot, so the planar array may be in an inefficient radiation regime where faster K-shell yield scaling with current (approaching I^4) might possibly
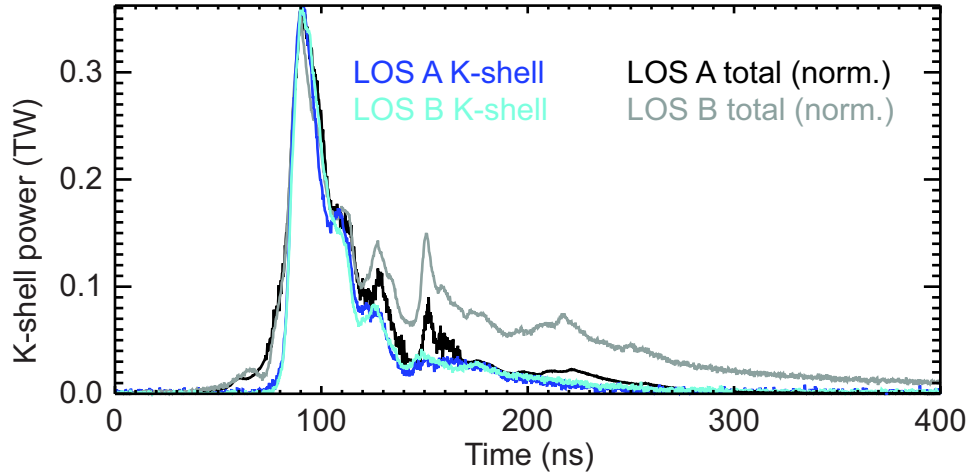
Figure 3.7. Al K-shell power measured with a 8 μm Be + 1 μm CH filtered PCD from Saturn shot 3688. 5 μm kimfol filtered XRD signals are shown normalized for comparison. Total K-shell yield 10.5 kJ (LOS A), 10.8 kJ (LOS B) was a small fraction of the total radiated yield 215 kJ (LOS A), 268 kJ (LOS B).

t

be expected [55, 56].

We note that this load does meet the $\eta > 2$ requirement for K-shell excitation, where η is the energy deposited in the plasma per ion divided by the minimum energy needed to ionize to the K-shell and is defined explicitly in Ref. [56]. Assuming the deposited energy equals the 0D-calculated **jxB**-coupled energy of 109 kJ for this load (Table 3.3) and using the total initial array mass, we calculate $\eta = 2.8$. The highest yields quoted in Ref. [5] were for cylindrical arrays with calculated η near 8 (and load mass near the soft mass break point), which may indicate that the planar array K-shell optimization will require higher η designs and correspondingly larger array widths in addition to higher current. It is unlikely that the full phenomenological K-shell scaling theory of Ref. [56] is applicable to planar arrays in its present form as coefficients appear that depend on load geometry and would have to be normalized to a database of planar array shots. Also, the scaling of the mass break point (which determines the point of transition in yield scaling from I^4 to I^2) with η was determined through numerical modeling of cylindrical loads [55], and some thought would have to be given as to whether this would hold with planar wire arrays.

The LOS C time-integrated crystal spectrometer (TIXTL) was fielded on shot 3688, and a spectrum was obtained showing the typical Al and Mg K-shell lines (e.g. Ly-α, He-α, Li-like satellites). The Al Ly-α line was observed to be of greater intensity than the Al He-α line, which implies high electron temperature likely in the $T_e > 500$ eV range, although detailed analysis is needed in order to be conclusive. Non-

LTE kinetic modeling in the manner of Ref. [57] is presently being carried out by A. S. Safronova (University of Nevada, Reno) to interpret these data and infer plasma conditions in the stagnated plasma. This analysis may confirm that suitable temperatures were obtained for efficient ionization to the K-shell. It will also be valuable to infer the ion density and (with pinhole images showing the pinch diameter) estimate the mass participation fraction in the K-shell emission. It would also be interesting to compare the measured density with that obtained in a typical cylindrical array Al 5056 implosion.

Chapter 4

Conclusion

A series of twelve shots were performed on the Saturn generator in which planar wire arrays were studied to provide initial data on their x-ray performance and dynamics at multi-MA current levels. Variations in implosion time, array width, load current, and wire material were investigated.

An ICF scheme employing planar wire arrays could benefit from a significant reduction in primary holhraum wall area by compressing the wire array from a cylinder into a plane, but a key question is how x-ray power scales in the 100 ns implosion regime above 1 MA. Peak x-ray powers of 10±2 TW at 3 MA were obtained on these shots, with a mass scan indicating ~100 ns as the optimal implosion time. A width scan indicated that x-ray power did drop with decreasing width; integrated modeling of a planar-array-driven hohlraum design is necessary to determine the optimum system size. Preliminary current scaling comparisons between these Saturn shots and 1 MA shots on the Zebra generator indicate that x-ray power could scale as I^2, however the data is sparse and scaling experiments at ≥ 6 MA should be conducted before drawing conclusions about scaling to high current levels on the Z machine. One shot produced 10 kJ of Al K-shell x-rays at 3.6 MA which may scale to values competitive with cylindrical arrays at higher currents and larger array widths.

Planar array modeling analogous to 0D implosion calculations with a coupled circuit model was used to aid the pre-shot load design, and to estimate coupled **jxB** energy and to consider implosion dynamics post-shot. Comparison of these simulations with measured yields and pulse shapes, along with time-resolved x-ray self-emission imaging of the implosion front, indicate that the **jxB**-coupled (kinetic) energy can likely explain the x-ray yield to the peak of the power pulse and perhaps the entire first x-ray peak, but are unlikely to explain the total x-ray yield. This is similar to observed behavior of cylindrical wire arrays.

Load dynamics appear to indicate that mass trails behind the first front to reach the axis at the start of rapid plasma heating. This may also be qualitatively similar to cylindrical wire arrays. Matching the measured planar array implosion time in a 0D calculation can require reducing the mass participation in the implosion by as much as 50%. The emitting implosion front is seen to stagnate ~10 ns prior to peak x-ray power, and the plasma column formed on axis grows in size after peak x-rays. These observations suggest that trailing mass may play a role in these

implosions, either serving to deliver additional kinetic energy later in time following the implosion front, or to switch the bulk of the current into the stagnated pinch, performing compressional PdV work or enhancing Ohmic heating at the time of peak x-rays.

Resistive heating in the presence of a Hall effect has been proposed for wire array loads as a significant source of energy input to the plasma [9]. The present study cannot address this in detail, but does provide experimental data for further theoretical consideration. In addition to consideration of Hall physics, 3D MHD studies of the load would be valuable in order to study the role of wire ablation, the location of the current, the importance of trailing mass in coupling additional kinetic energy and carrying current, the suitability of the 0D energy coupling models, and to determine if the plasma naturally evolves to exhibit the type of density contrast parameter that is required by the lower-dimensionality models including Hall effects.

Collaborative analysis is continuing, and results may be obtained in the near term that will aid in understanding the planar array implosion dynamics. Of particular note, the analysis of voltage monitor data from one shot may provide load inductance versus time. This would be helpful in corroborating the $\mathbf{jxB}$-coupled energy, and in inferring the location of the current at the time of stagnation (perhaps indicating whether there is trailing mass that is invisible to the x-ray self-emission imaging diagnostic). In addition, analysis of Al and Mg K-shell spectral lines from the one Al 5056 planar wire array may indicate what temperatures and densities are achievable in these loads.

Additional shots on Saturn could significantly enhance the present data set. The highest priority would be to design planar array load hardware with reduced inductance in order to increase the load current into the ∼6 MA range. Experimentally measured x-ray power in this regime is necessary to make a reasonably sound statement about how x-ray power might scale to current levels of interest to potential future experiments on the Z machine. Aluminum planar array shots at higher current and larger width could also be beneficial not only to assess K-shell yields, but also to spectroscopically diagnose plasma parameters and address stagnation physics. Valuable for cylindrical arrays as well, time-resolved spectroscopy would provide the maximum insight through addressing the accumulation of mass and heating on axis. Additional shot opportunities with tungsten as well as Al planar arrays would be helpful for understanding dynamics via x-ray pinhole imaging and voltage monitor measurements, and the x-ray radiography and inductance unfold techniques established on the Z machine could be used to further enhance understanding of pinch energetics should shots on that facility be possible in the future. Even a few shots on Z would provide definitive power scaling data to help motivate ICF concept studies using one or more planar wire arrays at high current.

References

[1] C. Deeney, M. R. Douglas, R. B. Spielman, et al. *Phys. Rev. Lett.*, 81:4883, 1998.

[2] R. B. Spielman, C. Deeney, G. A. Chandler, et al. *Phys. Plasmas*, 5:2105, 1998.

[3] M. K. Matzen, M. A. Sweeney, R. G. Adams, et al. *Phys. Plasmas*, 12:055503, 2005.

[4] T. W. L. Sanford, G. O. Allshouse, B. M. Marder, et al. *Phys. Rev. Lett.*, 77:5063, 1996.

[5] C. Deeney, T. J. Nash, R. B. Spielman, et al. *Phys. Plasmas*, 5:2431, 1998.

[6] V. L. Kantsyrev, L. I. Rudakov, A. S. Safronova, et al. *High Energy Dens. Phys.*, 3:136, 2007.

[7] V. V. Ivanov, V. I. Sotnikov, A. Haboub, et al. *Phys. Plasmas*, 14:032703, 2007.

[8] M. E. Cuneo, D. B. Sinars, D. E. Bliss, et al. *Phys. Rev. Lett.*, 94:225003, 2005.

[9] A. S. Chuvatin, L. I. Rudakov, and A. L. Velikovich. *AIP Conf. Proc.*, 808:343, 2006.

[10] J. P. Chittenden, S. V. Lebedev, C. A. Jennings, et al. *Plasma Phys. Control. Fusion*, 46:B457, 2004.

[11] S. N. Bland, S. V. Lebedev, J. P. Chittenden, et al. *Phys. Plasmas*, 11:4911, 2004.

[12] J. H. Hammer, M. Tabak, S. C. Wilks, et al. *Phys. Plasmas*, 6:2129, 1999.

[13] M. E. Cuneo, D. B. Sinars, E. M. Waisman, et al. *Phys. Plasmas*, 13:056318, 2006.

[14] R. A. Vesey, M. C. Herrmann, R. W. Lemke, et al. *Phys. Plasmas*, 14:056302, 2007.

[15] R. W. Lemke. Private communication, 2007.

[16] A. V. Shishlov, S. A. Chaikovsky, A. V. Fedunin, et al. Microsecond planar wire array implosions on the GIT-12 generator, Oral presentation 4A7. *34th IEEE International Conference on Plasma Science (ICOPS)*, 2007.

[17] B. Jones, C. Deeney, C. A. Coverdale, et al. *J. Quant. Spectrosc. Radiat. Transfer*, 99:341, 2006.

[18] C. Deeney, C. A. Coverdale, M. R. Douglas, et al. *Phys. Plasmas*, 6:3576, 1999.

[19] C. A. Coverdale, C. Deeney, M. R. Douglas, et al. *Phys. Rev. Lett.*, 88:065001, 2002.

[20] C. A. Coverdale, K. Mikkelson, C. Deeney, et al. The new 12" diameter convolute hardware at Saturn: Design, assessment, and first results. *J. Rad. Effects and Rad. Eng.*, submitted 2007.

[21] W. A. Stygar, H. C. Ives, D. L. Fehl, et al. *Phys. Rev. E*, 69:046403, 2004.

[22] M. G. Mazarakis, C. E. Deeney, M. R. Douglas, et al. *Plasma Devices Oper.*, 13:157, 2005.

[23] S. V. Lebedev, D. J. Ampleford, S. N. Bland, et al. Wire array z-pinch experiments at Imperial College. In *Proceedings of the 3rd International Conference on Inertial Fusion Sciences and Applications (IFSA 2003)*, page 730. American Nuclear Soc. Inc, La Grange Park, IL, USA, 2004.

[24] M. P. Desjarlais. Private communication, 2006.

[25] V. L. Kantsyrev. Private communication, 2007.

[26] K. W. Struve, T. H. Martin, R. B. Spielman, et al. Circuit-code modeling of the PBFA Z for z-pinch experiments. In *Digest of Technical Papers, 11th IEEE Int. Pulsed Power Conf., Baltimore, MD*, page 162. IEEE, 1997.

[27] A. A. Esaulov, A. L. Velikovich, V. L. Kantsyrev, et al. *Phys. Plasmas*, 13:120701, 2006.

[28] A. S. Chuvatin. Private communication, 2007.

[29] G. A. Chandler, C. Deeney, M. Cuneo, et al. *Rev. Sci. Instrum.*, 70:561, 1999.

[30] R. B. Spielman, C. Deeney, D. L. Fehl, et al. *Rev. Sci. Instrum.*, 70:651, 1999.

[31] Y. Maron. Private communication, 2007.

[32] T. J. Nash, M. S. Derzon, G. A. Chandler, et al. *Rev. Sci. Instrum.*, 72:1167, 2001.

[33] R. B. Spielman. *Rev. Sci. Instrum.*, 66:867, 1995.

[34] R. B. Spielman, L. E. Ruggles, R. E. Pepping, et al. *Rev. Sci. Instrum.*, 68:782, 1997.

[35] B. Jones, C. Deeney, A. Pirela, et al. *Rev. Sci. Instrum.*, 75:4029, 2004.

[36] B. Jones, C. Deeney, C. A. Coverdale, et al. *IEEE T. Plasma Sci.*, 34:213, 2006.

[37] B. Jones, C. Deeney, C. A. Coverdale, et al. *Rev. Sci. Instrum.*, 77:10E316, 2006.

[38] B. Jones, C. Deeney, C. J. Meyer, et al. *AIP Conf. Proc.*, 926:229, 2007.

[39] T. Nash, M. Derzon, R. Leeper, et al. *Rev. Sci. Instrum.*, 70:302, 1999.

[40] M. E. Cuneo, E. M. Waisman, S. V. Lebedev, et al. *Phys. Rev. E*, 71:046406, 2005.

[41] C. Deeney, T. J. Nash, R. B. Spielman, et al. *Phys. Rev. E*, 56:5945, 1997.

[42] K. G. Whitney, J. W. Thornhill, J. P. Apruzese, et al. *Phys. Plasmas*, 11:3700, 2004.

[43] D. L. Peterson, R. L. Bowers, K. D. McLenithan, et al. *Phys. Plasmas*, 5:3302, 1998.

[44] L. I. Rudakov, A. L. Velikovich, J. Davis, et al. *Phys. Rev. Lett.*, 84:3326, 2000.

[45] M. G. Haines, P. D. LePell, C. A. Coverdale, et al. *Phys. Rev. Lett.*, 96:075003, 2006.

[46] V. I. Sotnikov, V. V. Ivanov, T. E. Cowan, et al. Investigation of electromagnetic flute mode instability in a high beta z-pinch plasma. *IEEE T. Plasma Sci.*, 34:2239, 2006.

[47] B. S. Bauer, V. L. Kantsyrev, F. Winterberg, et al. *AIP Conf. Proc.*, 409:153, 1997.

[48] W. A. Stygar, M. E. Cuneo, R. A. Vesey, et al. *Phys. Rev. E*, 72:026404, 2005.

[49] M. G. Mazarakis, M. E. Cuneo, W. A. Stygar, et al. Faster, 80ns, current scaling experiments yield higher radiated x-ray power and approach quadratic dependence. In preparation, 2007.

[50] S. V. Lebedev, F. N. Beg, S. N. Bland, et al. *Phys. Plasmas*, 8:3734, 2001.

[51] S. V. Lebedev, D. J. Ampleford, S. N. Bland, et al. *Plasma Phys. Control. Fusion*, 47:A91, 2005.

[52] V. V. Ivanov, V. I Sotnikov, G. S. Sarkisov, et al. *Phys. Rev. Lett.*, 97:125001, 2006.

[53] B. Jones, C. A. Jennings, M. E. Cuneo, et al. Measurement of plasma temperature and density profiles, implosion velocity and kinetic energy in wire array z pinches, Poster presentation 3P107. *34th IEEE International Conference on Plasma Science (ICOPS)*, 2007.

[54] D. B. Sinars, M. E. Cuneo, E. P. Yu, et al. *Phys. Rev. Lett.*, 93:145002, 2004.

[55] J. W. Thornhill, K. G. Whitney, C. Deeney, et al. *Phys. Plasmas*, 1:321, 1994.

[56] J. W. Thornhill, A. L. Velikovich, R. W. Clark, et al. *IEEE T. Plasma Sci.*, 34:2377, 2006.

[57] A. Safronova, V. Kantsyrev, A. Esaulov, et al. *AIP Conf. Proc.*, 808:149, 2006.

DISTRIBUTION:

1   A.A. Esaulov
Nevada Terawatt Facility/372
University of Nevada, Reno
Reno, NV 89557

1   V.L. Kantsyrev
Physics Department/220
University of Nevada, Reno
Reno, NV 89557

1   A.S. Safronova
Physics Department/220
University of Nevada, Reno
Reno, NV 89557

1   V.V. Ivanov
Physics Department/220
University of Nevada, Reno
Reno, NV 89557

1   J. Kindel
Physics Department/220
University of Nevada, Reno
Reno, NV 89557

1   R.C. Mancini
Physics Department/220
University of Nevada, Reno
Reno, NV 89557

1   A.S. Chuvatin
Laboratoire de Physique et Technologie des Plasmas
Laboratoire du Centre National de la Recherche Scientifique
Ecole Polytechnique
91128 Palaiseau
France

1   L.I. Rudakov
Icarus Research
P.O. Box 30780
Bethesda, MD 20824-0780

1   J.W. Thornhill
Naval Research Laboratory
Plasma Physics Division
Radiation Hydrodynamics Branch
Code 6720
Washington, DC 20375

1   C. Deeney
Director, Office of Defense Science
NA-11/Forrestal Building
U.S. Department of Energy
1000 Independence Ave., S.W.
Washington, DC 20585

5	MS 1193	B. Jones, 1673
5	MS 1193	M.E. Cuneo, 1673
1	MS 1106	D.J. Ampleford, 1673
1	MS 1159	C.A. Coverdale, 1344
1	MS 1194	E.M. Waisman, 1673
1	MS 1186	R.A. Vesey, 1674
1	MS 1196	D.S. Nielsen, 1675
1	MS 1193	L.B. Nielsen-Weber, 1675
1	MS 1193	R.E. Hawn, 1675
1	MS 1179	J.D. Serrano, 1344
1	MS 1196	J.A. Torres, 1675
1	MS 1193	M. Jones, 1675
1	MS 1192	D.A. Graham, 1676
1	MS 1192	S.P. Toledo, 1676
1	MS 1106	R.K. Michaud, 1342
1	MS 1106	D.M. Abbate, 1342
1	MS 1193	M.D. Kernaghan, 1672
1	MS 1193	M. Vigil, 1675
1	MS 1168	D.H. Romero, 1646
1	MS 1186	M.F. Johnson, 1675
1	MS 1186	J.E. Garrity, 1675
1	MS 1193	M.R. Lopez, 1675
1	MS 1192	T.C. Wagoner, 1676

1	MS	1192	R.L. Mourning, 1676
1	MS	1194	J.K. Moore, 1676
1	MS	1194	W.E. Fowler, 1671
1	MS	1106	K.A. Mikkelson, 1342
1	MS	1106	B.P. Peyton, 1342
1	MS	1106	T.A. Meluso, 1342
1	MS	1106	B.M. Henderson, 1342
1	MS	1106	M.A. Torres, 1342
1	MS	1106	J.W. Gergel, Jr., 1342
1	MS	1190	M.K. Matzen, 1600
1	MS	1191	J.L. Porter, 1670
1	MS	1181	T.A. Mehlhorn, 1640
1	MS	1181	L.X. Schneider, 1650
1	MS	1178	D.D. Bloomquist, 1630
1	MS	1168	D.H. McDaniel, 1650
1	MS	1186	M.P. Desjarlais, 1640
1	MS	0125	J.P. VanDevender, 12101
1	MS	1179	M.A. Hedemann, 1340
1	MS	1159	J.W. Bryson, 1344
1	MS	1196	W.A. Stygar, 1671
1	MS	1193	B.W. Atherton, 1672
1	MS	1186	M. Herrmann, 1674
1	MS	1191	G.T. Leifeste, 1675
1	MS	1196	R.J. Leeper, 1677
1	MS	1193	B.V. Oliver, 1645
1	MS	1168	C.A. Hall, 1646
1	MS	1152	M.L. Kiefer, 1652

1 MS 1152   T.D. Pointon, 1652

1 MS 1168   P.D. LePell, 1673

1 MS 1186   T.A. Brunner, 1641

1 MS 1186   R.B. Campbell, 1641

1 MS 1186   K.R. Cochrane, 1641

1 MS 1186   C.J. Garasi, 1641

1 MS 1186   T.A. Haill, 1641

1 MS 1186   H.L. Hanshaw, 1641

1 MS 1186   C. Jennings, 1641

1 MS 1186   R.W. Lemke, 1641

1 MS 1186   E.P. Yu, 1641

1 MS 1186   P.J. Christenson, 1674

1 MS 1186   T.K. Mattsson, 1641

1 MS 1186   K. Peterson, 1674

1 MS 1186   A.B. Sefkow, 1674

1 MS 1186   S.E. Rosenthal, 1674

1 MS 1186   S.A. Slutz, 1674

1 MS 1186   R.C. Mancini, 1677

1 MS 1191   M.A. Sweeney, 1670

1 MS 1193   D.C. Rovang, 1645

1 MS 1194   J.R. Woodworth, 1671

1 MS 1193   G.R. Bennett, 1672

1 MS 1193   D.L. Hanson, 1673

1 MS 1193   D.B. Sinars, 1673

1 MS 1193   L.A. McPherson, Jr., 1675

1 MS 1186   D.M. Sachs, 1675

1 MS 1192   W.M. White, 1675

1	MS	1193	D.E. Bliss, 1672
1	MS	1194	M.G. Mazarakis, 1671
1	MS	1194	M.E. Savage, 1671
1	MS	1194	K.W. Struve, 1670
1	MS	1196	J.E. Bailey, 1677
1	MS	1196	G.A. Chandler, 1677
1	MS	1196	D.L. Fehl, 1677
1	MS	1196	T.J. Nash, 1677
1	MS	1196	R.E. Olson, 1677
1	MS	1196	G.A. Rochau, 1677
1	MS	1196	C.L. Ruiz, 1677
1	MS	1196	T.W.L. Sanford, 1677
			,
1	MS	0899	Technical Library, 9536 (electronic copy)
1	MS	0123	D. Chavez, LDRD Office, 1011